(2)

Naval Research Laboratory
Washington, DC 20375-5000

NRL Memorandum Report 6065

Design of a High Voltage Multi-Cavity 35 GHz Phase-Locked Gyrotron Oscillator

A. W. FLIFLET, S. H. GOLD AND W. M. MANHEIMER

High Power Electromagnetic Radiation Branch
Plasma Physics Division

November 1, 1988

Approved for public release; distribution unlimited.

SECURITY CLASSIFICATION OF THIS PAGE

REPORT DOCUMENTATION PAGE

Form Approved OMB No. 0704-0188

1a. REPORT SECURITY CLASSIFICATION UNCLASSIFIED	1b. RESTRICTIVE MARKINGS
2a. SECURITY CLASSIFICATION AUTHORITY 2b. DECLASSIFICATION / DOWNGRADING SCHEDULE	3. DISTRIBUTION / AVAILABILITY OF REPORT Approved for public release; distribution unlimited.
4. PERFORMING ORGANIZATION REPORT NUMBER(S) NRL Memorandum Report 6065	5. MONITORING ORGANIZATION REPORT NUMBER(S)
6a. NAME OF PERFORMING ORGANIZATION Naval Research Laboratory 6b. OFFICE SYMBOL (If applicable) Code 4740	7a. NAME OF MONITORING ORGANIZATION
6c. ADDRESS (City, State, and ZIP Code) Washington, DC 20375-5000	7b. ADDRESS (City, State, and ZIP Code)
8a. NAME OF FUNDING / SPONSORING ORGANIZATION 8b. OFFICE SYMBOL (If applicable)	9. PROCUREMENT INSTRUMENT IDENTIFICATION NUMBER
8c. ADDRESS (City, State, and ZIP Code)	10. SOURCE OF FUNDING NUMBERS PROGRAM ELEMENT NO / PROJECT NO / TASK NO / WORK UNIT ACCESSION NO

11. TITLE (Include Security Classification)
Design of a High Voltage Multi-Cavity 35 GHz Phase-Locked Gyrotron Oscillator

12. PERSONAL AUTHOR(S)
Fliflet, A.W., Gold, S.H. and Manheimer, W.M.

13a. TYPE OF REPORT	13b. TIME COVERED	14. DATE OF REPORT (Year, Month, Day)	15. PAGE COUNT
	FROM ____ TO ____	1988 November 1	59

16. SUPPLEMENTARY NOTATION

17. COSATI CODES			18. SUBJECT TERMS (Continue on reverse if necessary and identify by block number)
FIELD	GROUP	SUB-GROUP	Gyrotron; Phase-locked; Oscillator

19. ABSTRACT (Continue on reverse if necessary and identify by block number)

This paper describes the design for an experimental high power, phase-locked gyrotron oscillator. The electron beam is generated by a 1 MV pulseline accelerator, and the reference signal is provided by a 35 GHz, 20 kW magnetron. The expected output power is in the range of 1 to 10 MW. The design is based on a solid 1 MeV, 100 Amp, 4 mm electron beam with a momentum pitch ratio α of 0.75. The locking signal from the magnetron is introduced via a prebunching cavity. A second (passive) bunching cavity is used to increase the locking frequency bandwidth obtainable with a given locking power. The bunching cavities are designed to operate in the fundamental TE_{111} cylindrical cavity mode. Some competition from the TE_{112} higher order axial mode could not be avoided due to the constraint on the minimum drift tube diameter set by the requirement to propagate the electron beam. The bunching cavities include two axial slots to control the cavity Q factor and suppress competing modes. Additional slots and apertures are used to suppress oscillation

(Continues)

20. DISTRIBUTION / AVAILABILITY OF ABSTRACT ☒ UNCLASSIFIED/UNLIMITED ☐ SAME AS RPT ☐ DTIC USERS	21. ABSTRACT SECURITY CLASSIFICATION UNCLASSIFIED
22a. NAME OF RESPONSIBLE INDIVIDUAL Arne W. Fliflet	22b. TELEPHONE (Include Area Code) (202) 767-2469 22c. OFFICE SYMBOL Code 4742

DD Form 1473, JUN 86 Previous editions are obsolete. SECURITY CLASSIFICATION OF THIS PAGE

S/N 0102-LF-014-6603

19. ABSTRACTS (Continued)

in the drift spaces. The output cavity operates in the TE_{121} mode and is also slotted to reduce competing mode excitation. The maximum phase-locking bandwidth is estimated to be 0.1% and the time to achieve phase-locked operation is about 20 nsec which is consistent with the pulselength of the NRL VEBA accelerator.

CONTENTS

DESIGN OF A HIGH VOLTAGE MULTI-CAVITY 35 GHZ PHASE-LOCKED GYROTRON OSCILLATOR

I. Introduction

This paper describes the design for an experimental high power, phase-locked gyrotron oscillator. The electron beam is generated by a 1 MV pulseline accelerator, and the reference signal is provided by a 35 GHz, 20 kW magnetron. The expected output power is in the range of 1 to 10 MW. The experiment is intended to serve as a test bed for the development of very high peak power phase-locked gyrotron oscillators. These oscillators are of interest as sources for advanced high-accelerating-gradient RF accelerators and as sources for phased-array directed-energy antenna systems. The experiment should allow the investigation of important elements of the design of these devices and of the diagnostics required for demonstrating phase-locked operation under short pulse, low repetition-rate conditions.

A schematic of the experimental configuration is shown in Fig. 1. A solid 1 MeV, ~100 A electron beam is produced by the NRL VEBA pulseline accelerator, with a voltage pulse length (FWHM) of approximately 55 nsec and a voltage flat-top of approximately 30 nsec. The beam will be produced by a modified version of the VEBA diode previously used to produce a high quality, low transverse velocity beam for millimeter wavelength

Manuscript approved July 19, 1988.

free-electron laser (FEL) experiments. The required beam transverse momentum, the free energy source for the cyclotron resonance maser interaction, is produced initially by a bifilar helical wiggler and then increased to a final momentum pitch ratio α of approximately 0.75 by adiabatic compression of the axial magnetic field. The locking signal from the magnetron is introduced via a prebunching cavity. A second (passive) bunching cavity is used to increase the locking frequency bandwidth obtainable with a given locking power.

The bunching cavities are designed to operate in the fundamental TE_{111} cylindrical cavity mode. The use of this mode simplifies the problems of spurious mode excitation and cavity crosstalk which can occur when the bunching cavities are designed to operate in a higher order mode. Some competition from the TE_{112} higher order axial mode could not be avoided due to the constraint on the minimum drift tube diameter set by the requirement to propagate the electron beam. The bunching cavities include two axial slots to control the cavity Q factor and suppress competing modes. Additional slots and apertures are used to suppress oscillation in the drift spaces. The output cavity operates in the TE_{121} mode, since this mode is better matched to a 10 MW level output power than is the fundamental mode. The output cavity is also slotted to reduce competing mode excitation.

II. Phase-locking Bandwidth

A linear theory of gyrotron oscillator phase locking via a prebunching cavity has been presented by Manheimer (1987). The nonlinear theory of gyrotron phase locking has been investigated by Fliflet and Manheimer. As shown by Fliflet and Manheimer, a simple estimate for the locking bandwidth obtainable with a prebunching cavity is given by:

$$\frac{\Delta\omega}{\omega_o} \leq 2\sqrt{\pi}\,\frac{\mu I_G}{2QF}\,J_1(q)\,e^{-\left[\frac{\mu\Delta}{4}\right]^2}\,J_1'(\beta_{to}) \qquad (1)$$

where μ is the normalized interaction length, Δ is the normalized resonance detuning parameter, I_G is the normalized current, F is the normalized steady-state field amplitude, Q is the quality factor of the output cavity, J_1 is the regular Bessel function of order 1, J_1' is its derivative, q is the beam azimuthal phase bunching parameter (defined in Eq. 6 below), and β_{to} is the initial transverse velocity of the electron beam divided by c, the speed of light. The normalized gyrotron parameters are defined as in Danly and Temkin (1986). The Bessel function derivative on the right-hand side of Eq. (1) can be replaced by 0.5, to a good approximation, for moderate voltage devices ($V \leq 100$kV). Equation (1) assumes that the axial RF field profile in the cavity has a gaussian form given by $f(z)=\exp\{-[3^{1/2}(2z/d-1)]^2\}$ where z ranges from 0 to d and d is the effective interaction length in MKS units. The normalized

interaction length, and the detuning parameter for the fundamental harmonic interaction are defined in terms of physical parameters expressed in MKS units according to:

$$\mu = \pi \frac{\beta_{to}^2}{\beta_{zo}} \frac{d}{\lambda} \qquad (2)$$

$$\Delta = \frac{2}{\beta_{to}^2} \left(1 - \frac{\Omega}{\omega_o}\right) \qquad (3)$$

where β_{zo} is the axial beam velocity at the cavity input divided by c, ω_o and λ are the angular frequency and wavelength of the radiation, and Ω is the relativistic cyclotron frequency. For a linearly polarized TE_{1n} circular waveguide mode and an on-axis beam, the normalized wave amplitude and beam current for the fundamental harmonic interaction are given by:

$$F = \frac{2|e|}{m_o c^2} \frac{\beta_{to}^{-3}}{\gamma_o} \frac{r_w}{x'_{1n}} E \qquad (4)$$

$$I_G = \left[\frac{2}{\pi}\right]^{\frac{5}{2}} \frac{|e|\mu_o}{4m_o c} \frac{Q}{\gamma_o \beta_{to}^4} \frac{\lambda}{d} \frac{1}{(x'^2_{1n}-1)J_1^2(x'_{1n})} I_o \qquad (5)$$

where e is the electron charge, m_o is the electron rest mass, μ_o is the free space permeability, γ_o is the relativistic mass ratio of the beam prior to the interaction, r_w is the cavity wall

radius, E is the peak electric field at the beam, I_0 is the dc beam current, x'_{1n} is a zero of $J'_1(x)$, and $k_{1n} = x'_{1n}/r_w$ is the transverse wavenumber. Equations (4) and (5) assume that the electron beam is placed on a maximum of $J'_1(k_{1n}R_o)$, which optimizes the beam-RF wave coupling impedance for linearly polarized TE_{1n} modes, where R_o is the beam guiding center radius. Equation (1) neglects effects of axial velocity modulation caused by the interaction in the bunching cavity and the effects of initial beam velocity spread. As discussed by Manheimer (1987), the effect of beam velocity spread is to reduce the resonance detuning parameter at which a given locking bandwidth can be obtained. If the expected beam quality is obtained ($\Delta v_z/v_z < 5\%$) this effect should be small in the present experiment.

The interaction length for optimum oscillator efficiency corresponds to $\mu \sim 6$-12 in the high power regime. Maximum output power and frequency bandwidth are obtained by using low Q values of order 200 to 500. In their investigation of gyroklystron design optimization Ganguly and Chu (1981) define a phase parameter $\Phi \equiv \mu\Delta - \pi$, which represents the phase slippage of a beam electron relative to the RF field due to kinematic effects. High efficiency is obtained by choosing $\Phi \sim \pi$-2π for the output cavity. The bunching process is most efficient when $\Phi \lesssim 0$ for the bunching cavity. The detuning parameter Δ is usually the same for both cavities and high output cavity efficiency requires that $\Delta \sim 1$. These conditions can be satisfied by keeping the bunching cavity short, i.e., $\mu_B \sim 2$-3.

Equation (1) shows that the maximum possible bandwidth, according to perturbation theory, corresponds to the maximum value (0.58) of the Bessel function J_1. This maximum occurs for q=1.83. A bunching parameter this large is very difficult to achieve with a single bunching cavity but appears feasible with multiple bunching cavities.

III. Bunching Cavity Design

The electron beam produced by a pulseline accelerator is characterized by voltage ripple and shot-to-shot variation which affect the resonance detuning of the interaction. For this reason it was considered highly desirable for the bunching cavities to be as stable as possible. Stability is enhanced by choosing a short interaction length and a low Q factor. Using a low Q factor also increases the bunching cavity bandwidth, which ultimately limits the phase-locking bandwidth, but it decreases the bunching fields, and, hence, the beam bunching parameter q, obtainable for a given drive power. The bunching parameter and locking frequency bandwidth can be enhanced by adding a second (passive) bunching cavity as discussed in Section V.

The design parameters of the bunching and power cavities were obtained in two steps. First, possible design configurations were obtained based on idealized cylindrical cavities with sinusoidal RF field profiles. This led to preliminary cavity lengths and Q factors and allowed the investigation of possible competing modes. Next, realistic RF field profiles were

calculated numerically for actual cavity wall dimensions and the device operating parameters were recalculated. A small signal threshold current code for cylindrical gyrotron cavities, developed by Chu 1978, was used to investigate possible competing modes. Figure 2 shows a scan of Q × threshold beam power (QP_{th}) versus magnetic field at maximum voltage for the TE_{111} mode in the prebunching cavity and for possible competing modes. The calculations assume $d/\lambda=2$ and $x=v_t/v_z=0.75$. The TE_{11} modes interact at the first harmonic, the TE_{21} modes interact at the second harmonic, and the TE_{31} modes interact at the third harmonic. This figure shows significant competition from modes interacting at higher harmonics ($\omega \approx 2\Omega$, etc.), as well as from higher order axial modes interacting at the fundamental. Note that in this model the TE_{112} mode interaction occurs at a lower magnetic field than the TE_{111} mode interaction and that, for a given Q factor, the minimum threshold current is higher for the higher order axial mode. As such the TE_{112} mode would not appear to be an important competing mode. As discussed below, this situation changes when the effect of the relatively large drift tube radius is taken into account. The horizontal line labelled Q=200 denotes the e-beam power. Axial slots will be used to reduce competing mode Q factors as well as control the Q of the operating mode. The design calculations for the cavity slots and locking signal input coupler are described in Section IV. The calculations shown in Fig. 2 are for linear polarization and an axis-centered beam with no spread in electron trajectory guiding

centers. In this limit, which is a good approximation for the current beam parameters, the starting current for linear polarization is simply twice that for circular polarization.

A major design constraint for a fundamental mode, solid beam gyroklystron is the need to maintain adequate cavity isolation while providing sufficient clearance in the drift sections to propagate the beam. In the present case, the ratio of drift tube radius to cavity wall radius is $r_d/r_w = 0.8$. This means that the cavity RF fields are only weakly cut off in the drift tube and that evanescent fringe fields extend well into the drift tube region. This effect leads to an axial RF field profile which is more accurately modelled by a gaussian function. The axial RF field profile corresponding to particular cavity dimensions was obtained numerically using a computer code based on the weakly irregular waveguide theory developed in Fliflet and Read (1981), modified for evanescent boundary conditions at each end of the cavity. (This approach may somewhat overestimate the field leakage into the cutoff region because coupling to higher order evanescent modes, which will occur when there are sharp discontinuities in the cavity wall, is not included in the computer model.) This profile was then used in an electron trajectory integration code (Fliflet 1985) to determine the oscillation threshold current as a function of magnetic field. The length of the cavity above-cutoff section was varied to obtain a value for which the minimum threshold current for the TE_{111} mode is greater than the beam current. In this way, a TE_{111}

cavity design having a minimum cold beam threshold current of 150 Amp and a normalized length μ=1.9 for α=0.75 was obtained. The cavity wall and RF field profiles for this mode and the TE_{112} mode are shown in Fig. 3. The TE_{112} mode is the only higher order mode with TE_{11} mode symmetry in the bunching cavity. It is only slightly cut off in the drift tubes, and therefore has a much greater axial extent than the TE_{111} mode. The possibility of competition from this mode, which oscillates at about 40 GHz, is discussed below. Taking into account insertion losses, the power coupled into the TE_{111} mode is assumed to be 5 kW. This leads to a normalized field amplitude F_1=0.03 in the first bunching cavity for a total Q of 200.

The primary consideration in choosing the length of the drift tube separating the cavities was to provide adequate cavity isolation. In addition, it was considered prudent to keep the drift length short to minimize the deleterious effects of beam velocity spread. An effective drift tube length of μ_d=3 was chosen, where μ_d is the distance from the end of the bunching cavity to the entrance of the next cavity, normalized in accordance with Eq. (2). Actually, the boundary between the end of the cavity and the beginning of the drift tube is not well defined due to the strong fringe fields; however, this was taken into account in the calculations. The detuning parameter for a typical magnetic field of 32 kG is Δ=0.91. As shown in Tran et al. (1986), the bunching parameter for a single bunching cavity with these parameters can be calculated using:

$$q = \sqrt{\pi}\, F_1\, \mu_1\, e^{-\left[\frac{\Delta_1 \mu_1}{4}\right]^2} \left[\frac{\sqrt{3}}{2}\mu_1 + \mu_d\right] \qquad (6)$$

where parameters with a "1" subscript denote bunching cavity parameters. The result is q=0.39.

The resonant frequency of the TE_{112} mode in the bunching cavity is ~40 GHz and the mode is very weakly cut off in the drift-tube sections. This leads to a mode with a significantly longer axial extent than the TE_{111} mode as shown in Fig. 3. This in turn leads to a very low starting current for this mode and a shift in the resonance interaction to higher magnetic fields. The threshold oscillation current as a function of magnetic field at full operating voltage (1 MV) is shown in Fig. 4 for the TE_{111} and TE_{112} modes assuming realistic axial field profiles. Comparison of this figure with Fig. 2 shows that the magnetic field corresponding to the minimum threshold current is approximately the same for the TE_{111} mode in both cases; however, in the case of the TE_{112} mode, it has been shifted to a significantly higher value for the realistic field profile. The minimum TE_{112} mode threshold current for the realistic profile is also much lower than the operating current. (Note that L denotes the axial mode index in Figs. 2-4.) The threshold current for the TE_{121} output cavity mode based on a realistic axial field profile (Fliflet and Read 1981) is also shown in Fig. 4. This figure shows that the resonant magnetic field for this mode

occurs below values corresponding to the excitation of the TE_{112} bunching cavity mode. Thus the TE_{112} mode interaction should not occur at full operating voltage, but excitation of this mode is probable during the rise and fall of the voltage pulse.

A time-dependent, single RF mode simulation code discussed in Fliflet and Manheimer was used to investigate transient oscillations in the TE_{112} mode for an approximate VEBA voltage waveform. The beam current and momentum pitch ratio (α) were assumed to scale as $I \propto V^{1.33}$ and $\alpha \propto V$ as in previous work (Gold et al. 1987). Power generated in the TE_{112} mode in the prebunching cavities during the rise and fall of the voltage pulse is shown in Fig. 5 for magnetic fields of 31, 32, and 33 kG, respectively. Most of this power would be radiated from the cavity slots and apertures. The peak power developed in this mode can be substantial, up to several MW's for a 33 kG field, but in all cases no oscillation occurs during the voltage flat-top.

IV. Bunching Cavity Slot and Input Coupler Design

The first prebunching cavity must have a low value of Q to the desired TE_{111} mode, which will be injected into the cavity from the reference source, as well as to any other modes that might oscillate in the cavity, including modes that are resonant at higher harmonics of the cyclotron interaction. The Q value selected to achieve this was 200. Since this cavity is closed at each end, the Q factor for a simple cylindrically symmetric cavity would be determined by ohmic losses and by cavity losses

associated with the input coupling aperture. These determine the internal and external Q values, Q_i and Q_e respectively, with the total value of Q given by the expression $Q_T = Q_i Q_e / (Q_i + Q_e)$. Since the ohmic Q would normally be very large (>1000) unless specially resistive walls were used, achieving the required Q primarily with the coupling aperture would result in a highly overcoupled configuration ($\beta \gg 1$, where $\beta = Q_i / Q_e$). Furthermore, unless great care were taken with the location of the aperture, for a Q of 200 in the TE_{111} mode, the aperture might not load all possible oscillating modes sufficiently to prevent their oscillation. (In fact, it would not load at all those modes with linear polarization in the plane of the coupling apertures, so that a multiple aperture configuration might be required.)

For that reason, it was decided to load the cavity Q by means of a pair of opposing axial slots, in order to reduce the value of Q_i for the TE_{111} and TE_{112} modes to approximately 400. In that case, a coupling Q of 400 would yield a total Q of 200 at a coupling β of 1. An additional advantage to the use of a pair of opposing axial slots is that it permits a limited amount of "squash-tuning" of the resonant frequency of the bunching cavities. This capability, both for the bunching cavities and the output cavity, is important to create experimental flexibility because the predicted phase-locking bandwidth (see Section VIII) can be much smaller than the predicted frequency-pulling of the gyrotron interaction with respect to the cold cavity frequencies (see Section V).

Figure 6 shows calculated values of Q_i as a function of slot angle for the TE_{11} mode as well as for several possible competing modes. These calculations were carried out using a theory and computer code described in McDonald et al. (1986), and assume that the slot extends wherever the mode of interest has substantial RF fields, so that the calculation is reduced to a two-dimensional boundary-value problem. Achieving a Q_i of 400 for the preferred linear polarization of the TE_{111} mode (i.e., the mode polarized along the slot plane) by means of axial slots requires a full slot angle of 44°. (The predicted Q of the orthogonal linear polarization is less than 5.) This slot angle reduces the Q of the competing TE_{21} and TE_{31} to 85 and 34, respectively, and the Q of the TM_{01} mode to 65. (The TM_{01} mode was of possible concern, because it was not initially clear if axial wall slots would substantially load a mode without azimuthal wall currents.) In order to ensure that the TE_{111} coupling hole would also substantially load the TE_{112} mode, the coupling aperture was placed one-third of the distance from the end of the cavity, rather than at the cavity midplane, as shown in Fig. 3.

Figure 3 shows calculated axial RF-field profiles for the TE_{111} and TE_{112} modes for one of the prebunching cavities as well as the location of the large number of apertures and slots used both to suppress higher-order transverse modes, and to linearly-polarize and control the Q of the desired TE_{111} mode and the competing TE_{112} mode. As discussed above, the drift spaces are

very weakly cut off to these modes, so that the fields extend well into the drift spaces separating the cavities. Thus, the effective RF cavity extends well beyond the nominal cavity length defined by the enlarged diameter section. The length of the main 44° axial slots of the cavity region is three times the length of the enlarged section of the cavity, in order to extend everywhere that the TE_{111} mode has substantial rf fields. As Fig. 3 shows, the TE_{112} mode extends much further into the cutoff region, and has substantial fields beyond the ends of the main cavity slots. In order to further suppress the TE_{112} mode, additional pairs of "keyhole" slots were placed in the walls of the cutoff section, beginning just beyond the main cavity slots, but at an angle of 90° from them. These slots are narrower (~40° full angle) at the ends nearest the cavities, in order not to load down the TE_{111} mode excessively, and open up into large apertures (diameters approximately equal to the cutoff section diameter) at the ends farthest from the cavities, in order to very effectively suppress modes polarized along the plane of the main cavity slots. The combination of large slots at 90° intervals in different regions of the cutoff section helps both to limit the spatial extent of the rf fields of the TE_{112} mode of the cavity, and also to substantially lower the Q of the TE_{11} mode of the drift spaces, of any polarization, as well as of other modes that might occur at higher harmonics of the cyclotron frequency, in order to prevent the build-up of oscillation in these regions. Figure 7

shows the result of a preliminary cold test of one of the bunching cavities.

V. Effect of Adding a Second Bunching Cavity

The realization of maximum phase-locking bandwidth requires a bunching parameter of at least 1.8 as discussed in Section II. This is a factor of ~5 greater than that which can be achieved with a single bunching cavity using the available drive power, since in this case, as discussed above, $q \lesssim 0.4$. The bunching parameter can be increased considerably by adding a second bunching cavity. The principle is the same as for conventional klystrons: The ac current induced on the beam by the RF fields in the first cavity induce much stronger fields in the second cavity. These fields in turn enhance the bunching of the beam. As shown in Tran et al. (1986), small-signal gyroklystron theory can be used to calculate the induced field F_2 in the second cavity:

$$F_2 = \sqrt{\pi}\, I_{G2}\, \mu_2\, e^{-x_2^2}\, J_1(q_2)/\sqrt{1+\delta^2} \qquad (7)$$

where $x_2 = \mu_2 \Delta/4$, $\delta = 2Q(\omega_o - \omega_{b1})/\omega_o$ and q_2 is the bunching parameter at the input to the second cavity. The frequency ω_o is the locking signal frequency and ω_{b1} is the beam-loaded resonant frequency of the second cavity. Since the bunching cavities are identical in the present design, $I_{G2} = I_{G1} = 1.1$ and $\mu_2 = \mu_1 = 1.9$. The beam-loaded oscillation frequency of the TE_{111} mode, expressed as

a shift relative to the cold cavity resonant frequency, is shown in Fig. 8 for gaussian (μ=1.9) and realistic axial mode profiles. These results were obtained using the time-dependent simulation code discussed in Fliflet and Manheimer for RF field amplitudes in the small-signal regime. The realistic profile leads to a frequency shift of 0.5% for B=32 kG, while the gaussian profile gives a shift of 0.7%. The gaussian profile length parameter was chosen to give a good fit to the minimum TE_{111} mode starting current determined using the realistic profile. However, the realistic profile frequency shift is expected to be more accurate. Since the maximum phase-locking bandwidth is about 0.1%, the beam-loaded frequency shift must be taken into account in the circuit design. The maximum induced field amplitude in the second bunching cavity for an on-resonance drive signal is shown in Fig. 9 as a function of magnetic field for q_2=0.3. This value of q_2 is about 75% of the value predicted by Eq.(6) [q=0.39] in order to allow for effects such as velocity spread which may reduce the effective bunching. Figure 9 shows $F_2 \simeq 0.47$ for B=32 kG, which is an order of magnitude higher than the field induced in the first cavity by a 5 kW locking signal. This analysis is supported by time-dependent simulations (Fliflet and Manheimer) for B=32 kG. The solid dot shows the result of a simulation based on the realistic axial mode profile and the open circle shows the result for a simulation using a gaussian profile (μ=1.9). As shown in the figure, the gaussian profile simulation is about 11% lower than the estimate based on Eq. (7) and the

realistic profile simulation is about 17% higher. These results are considered to validate Eq. (7), which is very useful for parameter optimization studies. Figure 10 shows the induced field amplitude in the second bunching cavity as a function of the drive frequency expressed as a shift relative to the beam-loaded resonant frequency. The curves labelled "RP" and "GP" correspond to simulation results for realistic and gaussian profiles, respectively, and the curve labelled "analytic" corresponds to Eq. (7). The calculations assume B=32kG and q=0.3.

VI. Output Cavity Design

The TE_{121} mode output cavity is formed by a length of cylindrical waveguide followed by a 5° uptaper. In most of the design analyses, the cavity axial mode profile is represented by a gaussian with an effective length μ=4.5. Thus, the length is less than optimum for highest efficiency. However, a longer cavity would shift the optimum operating point to higher magnetic fields which, in turn, would increase the likelihood of competition from the TE_{112} mode in the bunching cavities. A short cavity is also better matched for high power operation. The diffraction output Q factor is calculated to be approximately 400 using the theory presented in Fliflet and Read (1981). The numerically computed axial cavity profile for the output cavity is shown in Fig. 11.

A scan of QP_{thr} versus magnetic field is shown in Fig. 12 for the TE_{121} mode and competing modes. The calculation assumes a sinusoidal profile with length d=4.5λ and linear polarization. The TE_{12} modes interact at the first harmonic, the TE_{23} modes interact at the second harmonic, and the TE_{34} modes interact at the third harmonic. The horizontal line shows the beam power corresponding to Q=400. The line is clearly well above the oscillation threshold for the TE_{121} mode. Figure 12 indicates that potential competing modes include TE_{23} modes interacting at the second harmonic and higher order TE_{12} axial modes interacting at the fundamental. The modes supporting the higher order harmonic interactions are discriminated against by the addition of axial slots. The higher order axial modes are discriminated against by the diffraction output coupling.

The axial slot angle is chosen such that the axial slots have minimal effect on the TE_{121} mode while significantly loading competing modes. The numerically calculated curves of threshold current versus magnetic field, based on realistic RF field profiles for the bunching and output cavities, are shown in Fig. 4. The oscillation threshold current based on the realistic axial profile for the output cavity is compared in Fig. 13 with the result obtained using the time-dependent simulation code with a gaussian profile of length μ=4.5. The two calculations are in good agreement with respect to the minimum threshold current, but differ in shape particularly at the high magnetic fields. In addition to the difference in the profiles themselves, this

difference is attributed in part to a more accurate treatment of the beam-loaded frequency shift in the time-dependent code than in the steady-state code (Fliflet 1985) used for the realistic profile calculation.

VII. Output Cavity Slot Design

The output cavity Q should be determined principally by the output coupling, so that substantial energy will not flow out of the slots. The intrinsic Q of the unslotted output cavity is approximately 400. Fig. 14 shows the calculated "slot Q" versus slot half-angle for the output cavity. A full slot angle of 30° was selected to yield a slot Q of ~3000 for the preferred polarization, thus lowering the overall cavity Q to approximately 350, while effectively eliminating the orthogonal linear polarization. This slot angle yields a slot Q factor of 394 for the TE_{231} mode for an overall Q factor of 198 for this mode. As discussed in Section IV with respect to the bunching cavities, the slots also permit a modest amount of squash-tuning of the output cavity. The results of a preliminary cold test of the output cavity, showing the result of its squash-tuning, are given in Fig. 15.

The three microwave cavities and the connecting drift sections are shown to scale in Fig. 16. Because of the cavity slots, a separate vacuum enclosure surrounds the cavities. The vacuum enclosure is lined with microwave absorber, and is

designed to isolate the three cavities from each other, in order to avoid the possibility of undesired feedback.

VIII. Bandwidth Estimate

The free-running oscillator (FRO) parameters for the output cavity are shown as a function of magnetic field in Fig. 17. These parameters include the normalized RF-field amplitude, the beam-loaded frequency shift relative to the cold cavity frequency, the ratio of the beam current to the threshold beam current, and the electronic efficiency. As shown in Fig. 17, the peak efficiency of 13% occurs at B=32 kG and corresponds to a detuning parameter Δ=0.91 and field amplitude F=0.43. The beam-loaded frequency shift is 0.1% at 32 kG and increases with magnetic field. The normalized beam current for the output cavity is I_{a3}=0.35. Based on these parameters, the locking frequency bandwidth of the device can be estimated using the theory outlined in Section II. Assuming optimum bunching, the Bessel function in Eq. (1) can be replaced by 0.58 to obtain an upper bound on the achievable bandwidth according to linear theory. The result is shown in Fig. 18 as a function of magnetic field. At B=32kG, the predicted bandwidth is 0.16%. As shown in Fig. 18, the bandwidth is an increasing function of the magnetic field. Some increase in bandwidth could therefore be achieved by increasing the magnetic field at the cost of somewhat reduced efficiency.

The analytical results for the locking frequency bandwidth are supported by simulations using the time-dependent slow-time-scale (STS) code described in Fliflet and Manheimer. The simulations do not account for spreads in beam energy, electron orbit guiding center, or axial velocity. The efficiency is not expected to be sensitive to such effects; however, the locking bandwidth would be reduced by excessive velocity spread, i.e., greater than 5%. Code results (which are not based on perturbation theory) are shown in Figs. 19 and 20 for the output cavity driven by a beam with $q=2.0$. This value of q was chosen as representative of optimal bunching in the nonlinear regime, based on a limited parameter search using the code. (The optimal value predicted by linear theory is $q=1.83$.) A gaussian axial mode with $\mu=4.5$ is used in the calculations. Figure 19 shows results for an idealized flat voltage pulse including the driven oscillator efficiency, operating frequency expressed as a shift relative to the drive frequency, and the phase of the RF output. The normalized locking frequency shift is shifted 0.1% from the FRO frequency and the magnetic field is 32 kG. The efficiency of the driven oscillator is 17.5 percent and phase-locked operation is achieved within 20 nsec. The corresponding results for a typical, somewhat smoothed voltage waveform for the VEBA accelerator are shown in Fig. 20.

IX. Beam Formation

In order to form a cold, solid electron beam with an $\alpha \sim 0.75$, a "helix-gun" approach was chosen, in which a cold 100 A electron beam is produced by beam aperturing of a plasma-induced field emission diode, and the required beam α is induced by transit through a helical wiggler magnetic field followed by adiabatic compression of the applied axial magnetic field. The diode used in this device is derived from the diode used in the VEBA FEL experiment (Jackson et al. 1983). This approach is illustrated schematically in Fig.1. Based on the amplitude of the axial magnetic field in the vicinity of the diode, a helix period of 4 cm was selected.

There are two basic approaches to "pumping up" the transverse momentum of an electron beam with a helical wiggler magnet. In the first approach, an untapered wiggler of fixed length is used to resonantly pump the transverse momentum. In the second approach, a tapered "adiabatic entry" wiggler is used to inject the beam into wiggler orbits closely approximating ideal, constant axial velocity wiggler orbits, and then the wiggler is abruptly terminated, releasing the electrons into the uniform axial field with the same value of transverse momentum that they had developed within the wiggler. Either approach should work in the current experiment. The detailed design of the beam-forming system will be the subject of a future report.

X. Summary

In summary, a circuit design has been obtained for a phase-locked intense beam gyrotron oscillator with a locking frequency bandwidth of ~0.1%. The effective gain of output power to the locking power needed to achieve this bandwidth is about 28 dB. The circuit makes use of a novel arrangement of slots and apertures to control the Q of the bunching cavities and to prevent oscillation in spurious modes. K_a-Band cold test cavities have been constructed and have shown the desired combinations of Q-values, center frequencies, and frequency tunability. A method has been identified to produce an electron beam with the desired current, α, and velocity spread. The successful conclusion of this design effort, and our success in fabricating cold test cavities with the desired combination of properties, points the way to an experimental test of our design for a high voltage multi-cavity 35 GHz phase-locked gyrotron oscillator in the near future.

XI. ACKNOWLEDGMENT

We are grateful for useful discussions with a number of our colleagues, including D.A. Kirkpatrick, R.B. McCowan, A.K. Ganguly, and V.L. Granatstein, and A.T. Lin. A.K. Kinkead assisted in the fabrication of the cold test cavities. This work was supported in part by the Office of Innovative Science and Technology of the Strategic Defense Initiative Organization, and

managed by the Harry Diamond Laboratories, and in part by the Office of Naval Research.

REFERENCES

Chu, K.R., 1978, Theory of electron cyclotron maser interaction in a cavity at the harmonic frequencies, Phys. Fluids, 21, 2354.

Danly, B.G., and Temkin, R.J., 1986, Generalized nonlinear harmonic gyrotron theory, Phys. Fluids, 29, 561-567.

Fliflet, A.W., 1985, Scaling calculations for a relativistic gyrotron, NRL Memorandum Report 5598.

Fliflet, A.W., and Manheimer, W.M., Nonlinear theory of phase locking gyrotron oscillators driven by an external signal, submitted to Phys. Rev. A.

Fliflet, A.W., and Read, M.E., 1981, Use of weakly irregular waveguide theory to calculate eigenfrequencies, Q values, and RF field functions for gyrotron oscillators, Int. J. Electron., 51, 475-484.

Ganguly, A.K., and Chu, K.R., 1981, Analysis of two-cavity gyroklystron," Int. J. Electron., 51, 503-520.

Gold, S.H., Fliflet, A.W., Manheimer, W.M., McCowan, R.B., Black, W.M., Lee, R.C., Granatstein, V.L., Kinkead, A.K., Hardesty, D.L., and Sucy, M., 1987, High peak power Ka-Band gyrotron oscillator experiment, Phys. Fluids, 30, 2226-2238.

Jackson, R.H., Gold, S.H., Parker, R.K., Freund, H.P., Efthimion, P.C., Granatstein, V.L., Herndon, M., Kinkead, A.K., Kosakowski, J.E. and Kwan, T.J.T., 1983, Design and operation of

a collective millimeter-wave free-electron laser, IEEE J. Quantum Electron., QE-19, 346-356.

Manheimer, W.M., 1987, Theory of the multi-cavity phase locked gyrotron oscillator, Int. J. Electron., 63, 29-47.

McDonald, S., Finn, J.M., and Manheimer, W.M., 1986, Boundary integral method for computing eigenfunctions in slotted gyrotron cavities of arbitrary cross-sections, Int. J. Electron., 61, 795-822.

Tran, T.M., Danly, B.G., Kreischer, K.E., Schutkeker, J.B., and Temkin, R.J., 1986, Optimization of gyroklystron efficiency, Phys. Fluids, 29, 1274-1281.

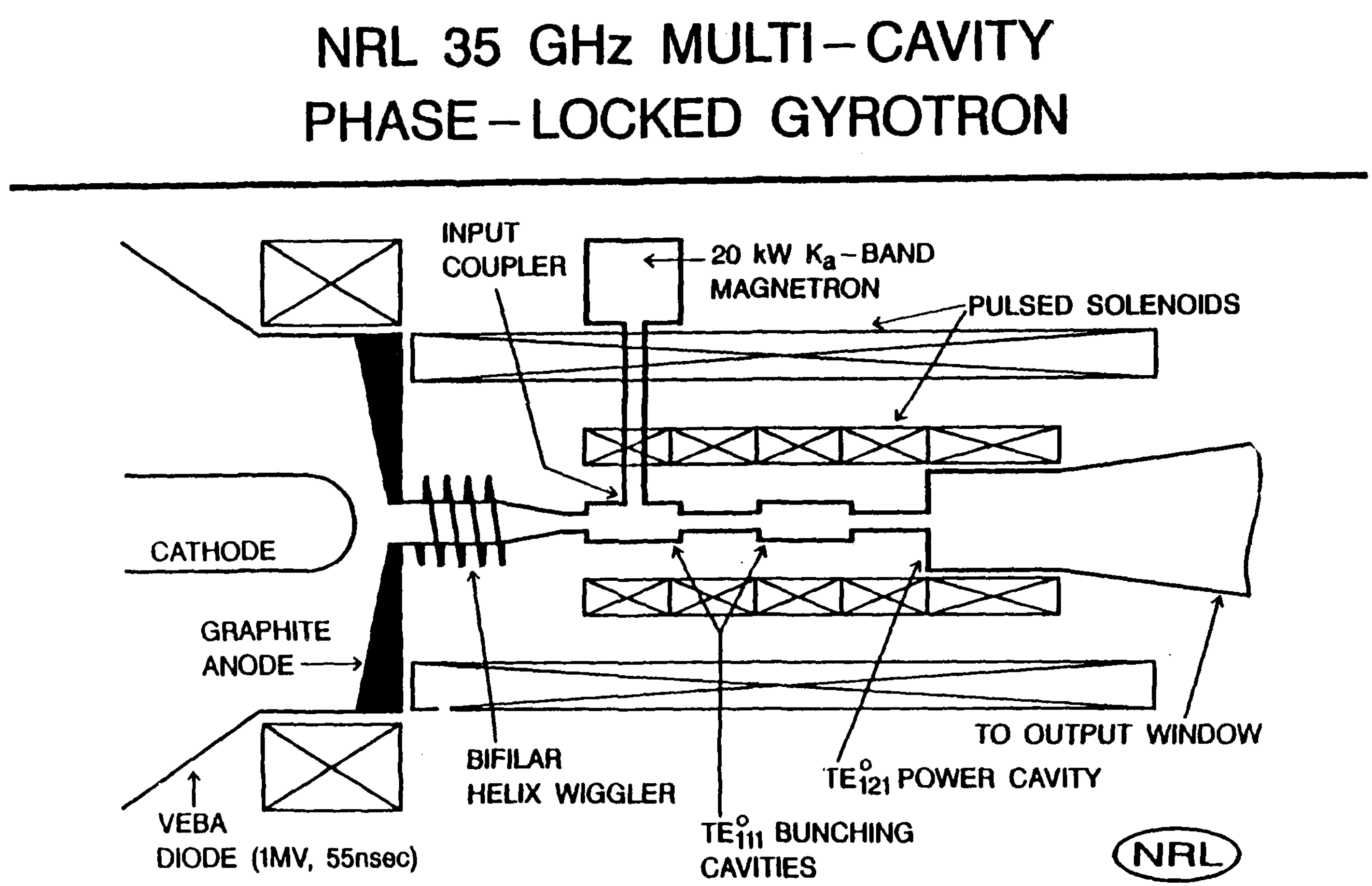

Fig. 1. Schematic of the VEBA three-cavity phase-locking experiment, showing the arrangement of the diode, wiggler, and microwave cavities.

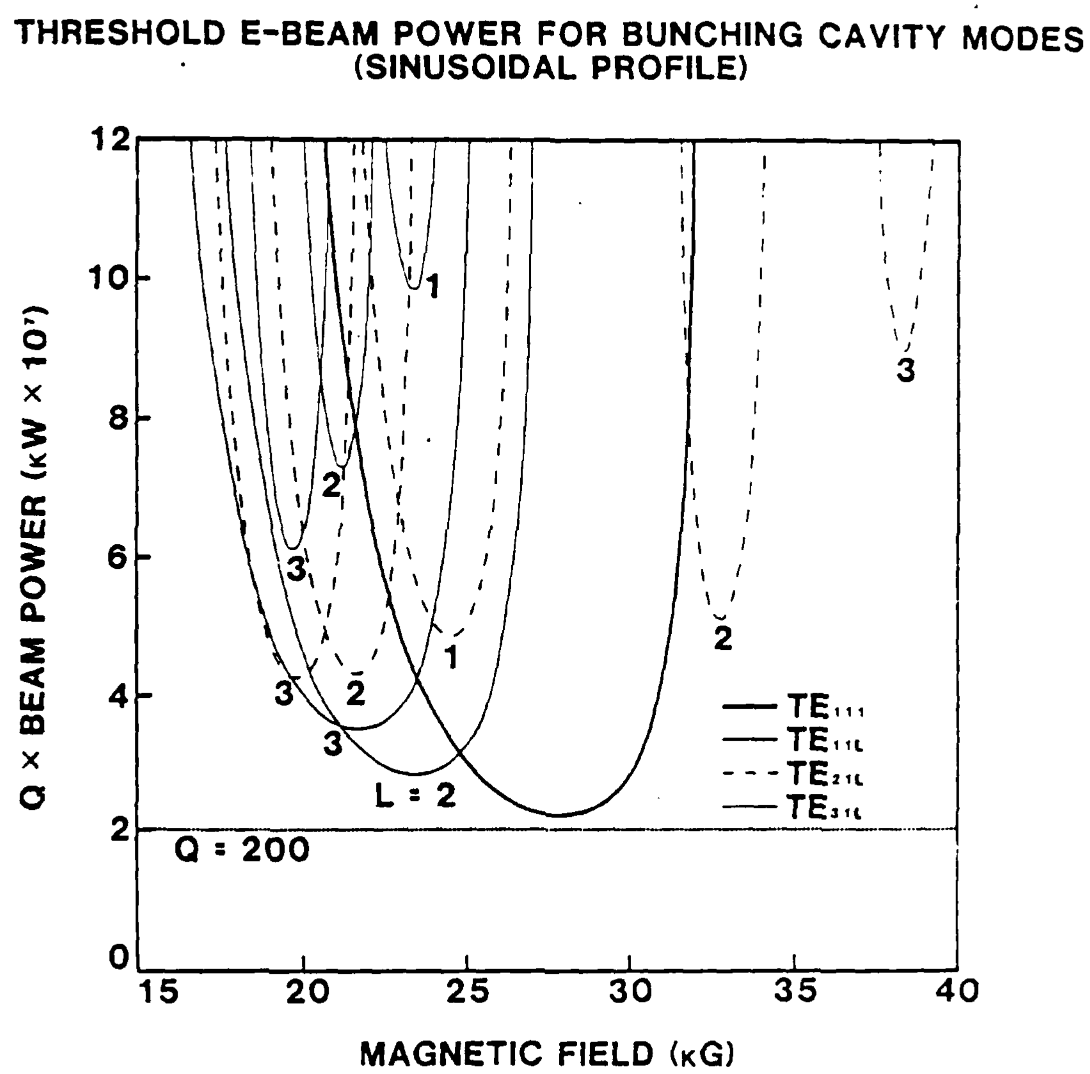

Fig. 2. Scan of Q x threshold beam power versus magnetic field for the TE_{111} mode and competing modes in the bunching cavity. The calculations assume a sinusoidal axial RF field profile with $L/\lambda=2$, circular polarization, and $\alpha=0.75$. The TE_{11} modes interact at the first harmonic, the TE_{21} modes interact at the second harmonic, and the TE_{31} modes interact at the third harmonic.

PREBUNCHING CAVITY SCHEMATIC AND AXIAL PROFILE FUNCTIONS

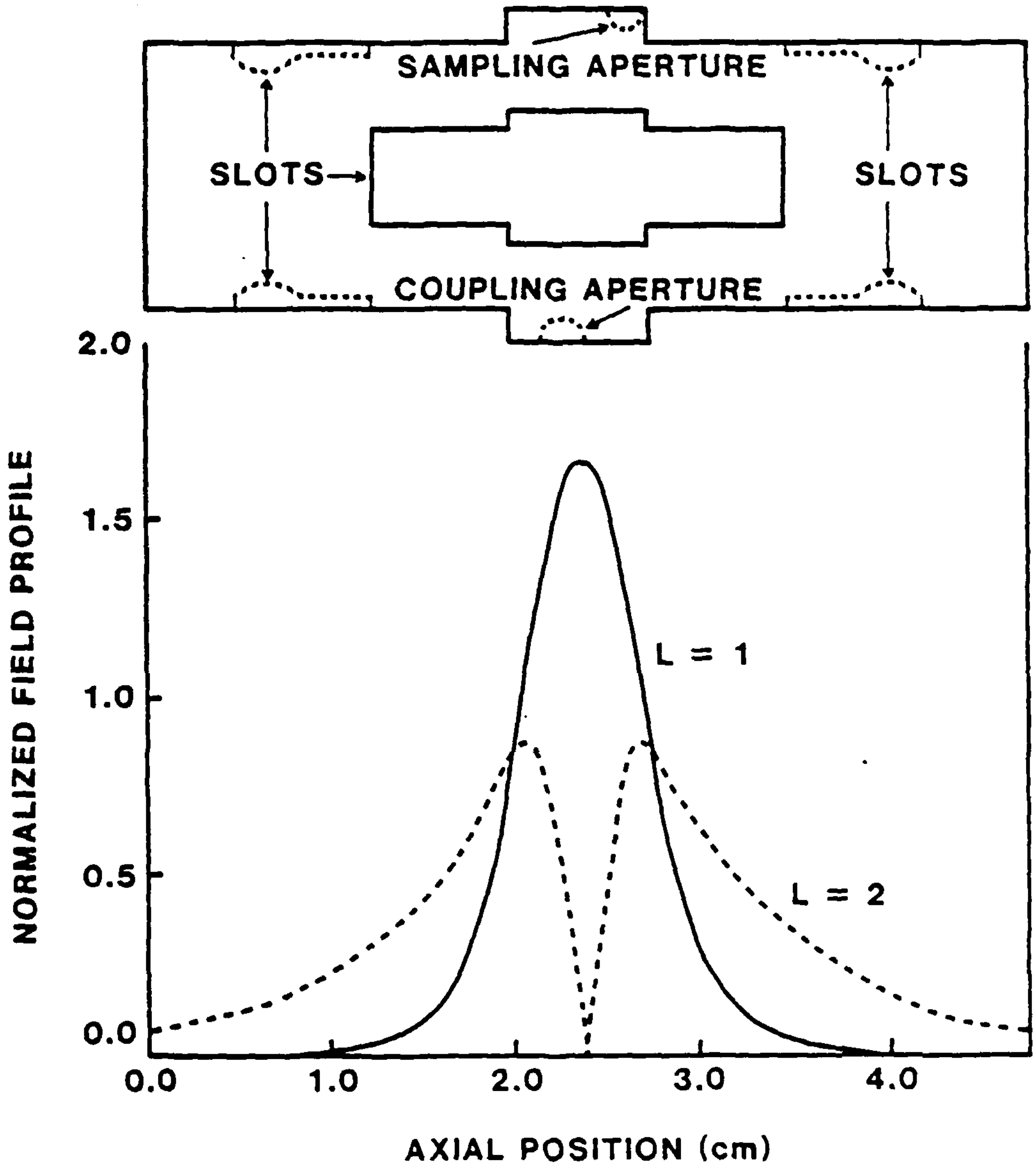

Fig. 3. Calculated axial profile functions for the TE_{111} and TE_{112} modes of the prebunching cavities, indicating the location of apertures and slots. (The calculated profiles do not include the effects of the four "keyhole" slots, which are expected to suppress the wings of the L=2 axial profile function.)

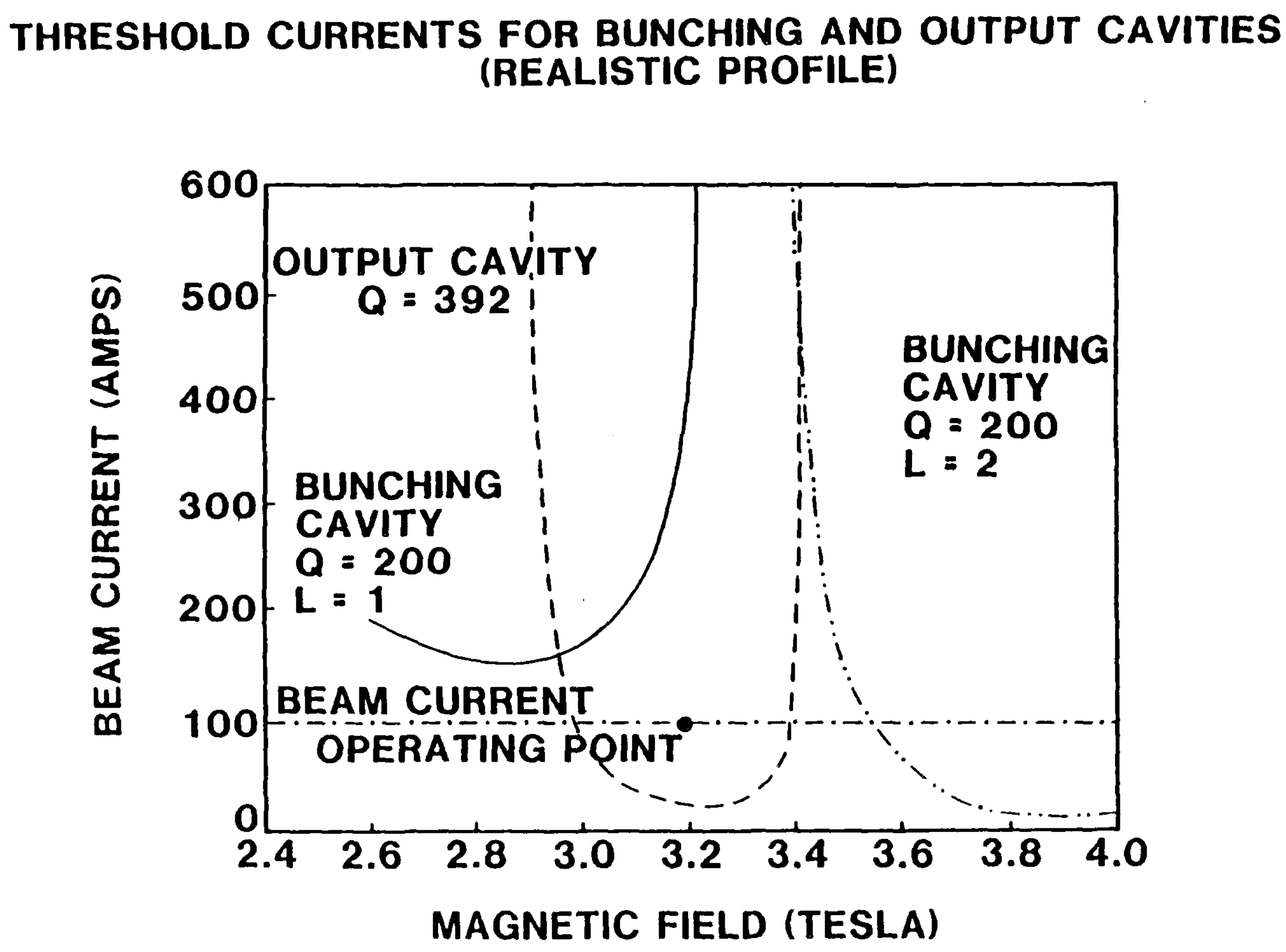

Fig. 4. Threshold current curves for dominant modes in the bunching and output cavities based on realistic axial RF field profiles.

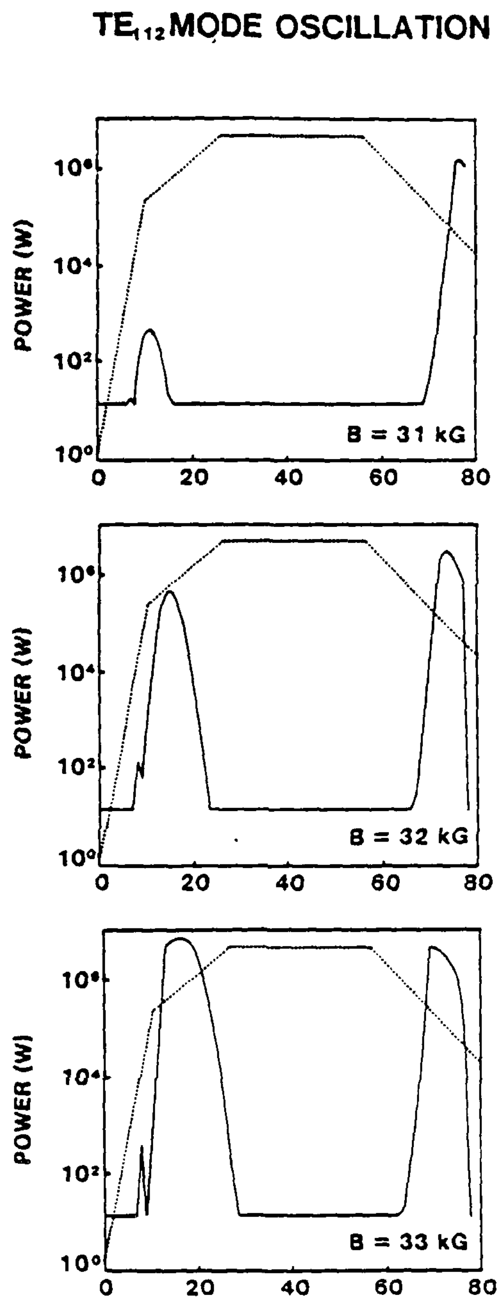

Fig. 5. Time evolution of RF power produced by TE_{112} self-oscillation in a bunching cavityfor three magnetic fields: B = 31 kG, B = 32 kG, and B = 33 kG.

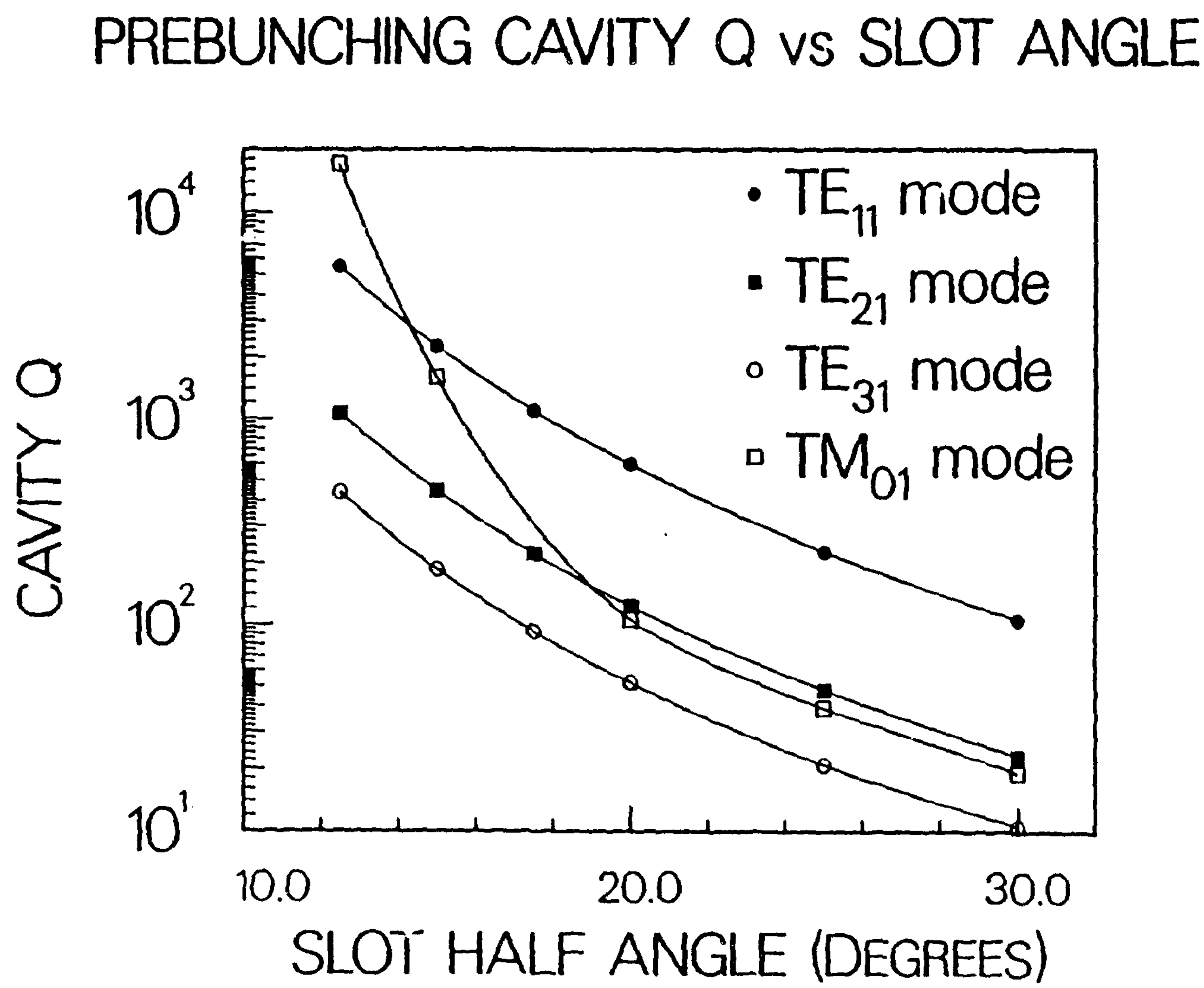

Fig. 6. Calculated Q-value vs slot half-angle for the TE_{11} mode and for possible competing modes in the prebunching cavities.

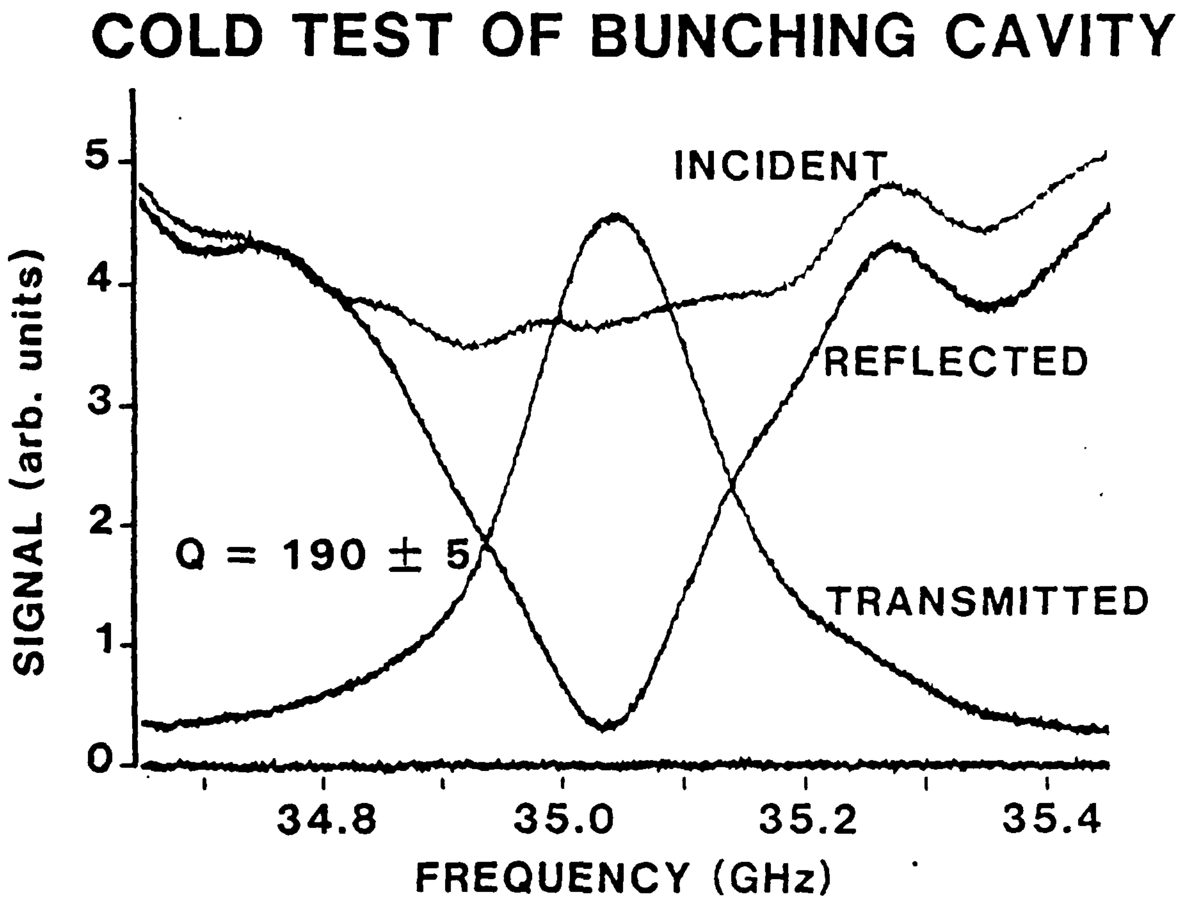

Fig. 7. Cold test of the TE_{111} resonance of one of the bunching cavities, showing incident and reflected signals at the coupling aperture, and the transmitted signal measured by the sampling aperture, which is proportional to the rf power coupled into the cavity. (The true zero point for these measurements is slightly displaced from the nominal zero due to a biasing effect introduced by a lock-in amplifier used to process the detected signals.)

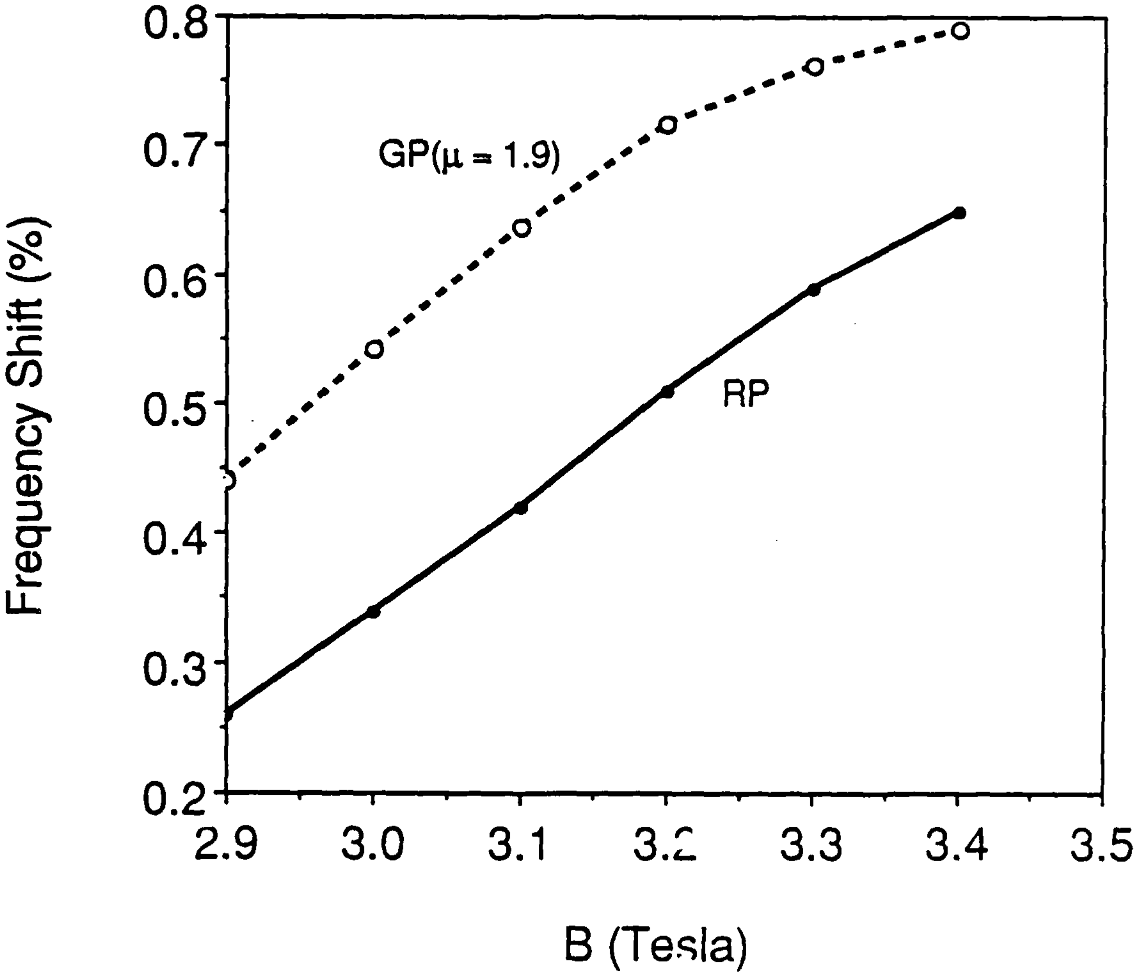

Fig. 8. Beam-loaded shift in resonant frequency for the TE_{111} mode in the bunching cavities. The curve labelled GP corresponds to a gaussian axial profile and the curve labelled RP corresponds to the realistic profile.

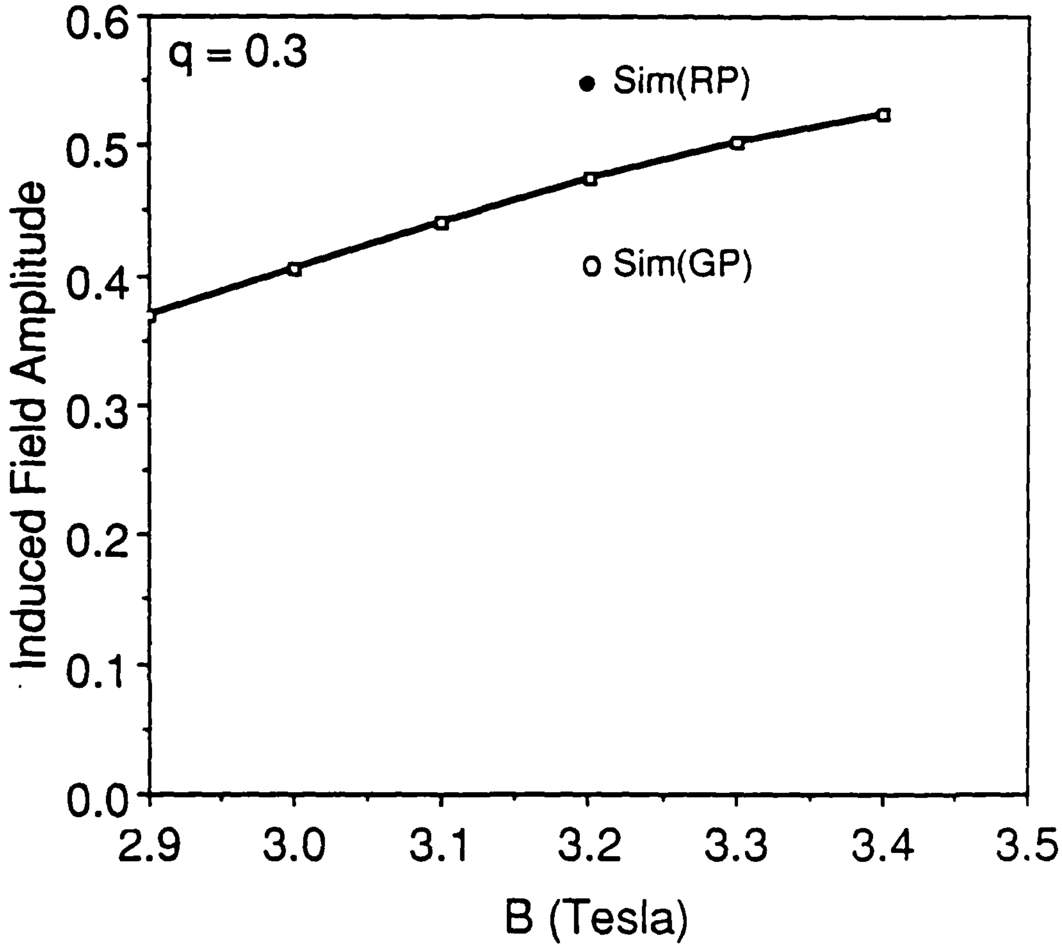

Fig. 9. Maximum induced field amplitude in second bunching cavity for q = 0.3. The solid curve is based on Eq. (7). The solid dot is the simulation result using the realistic axial profile and the open circle is the simulation result using a gaussian profile.

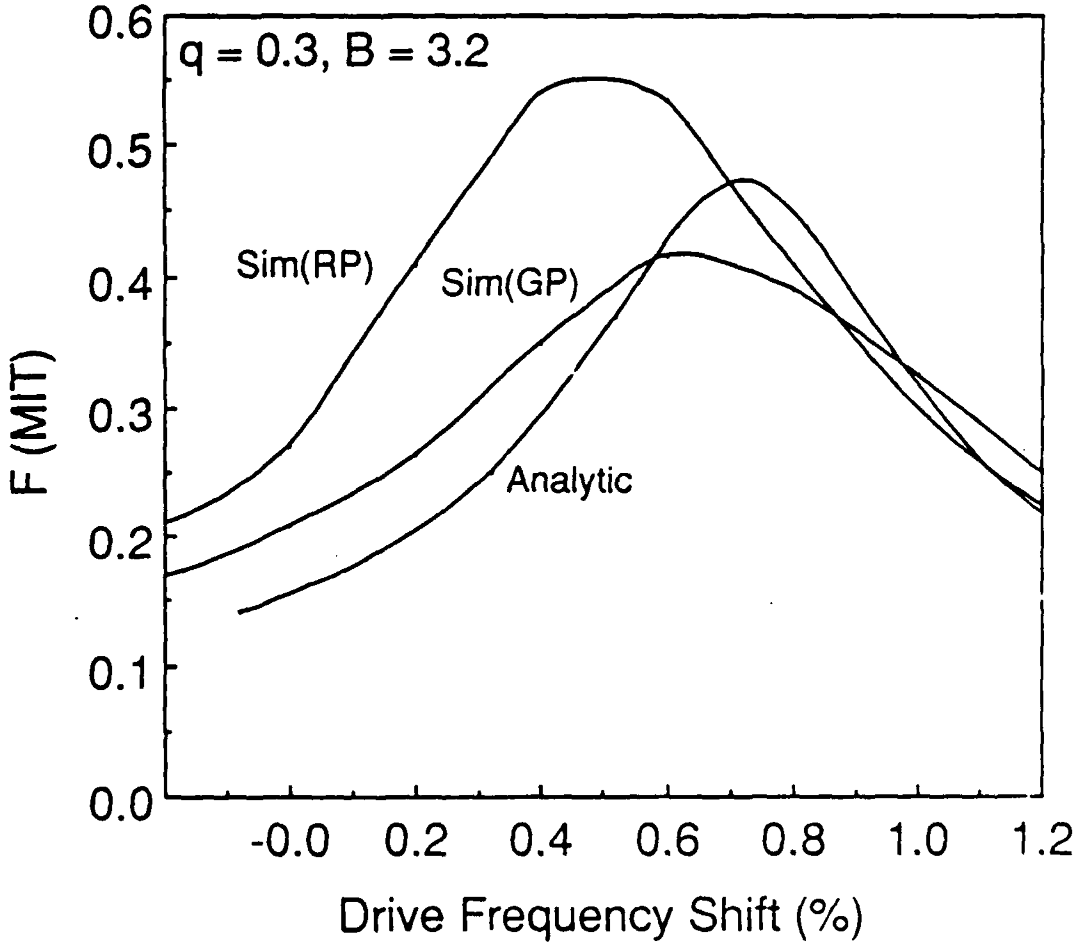

Fig. 10. Induced field amplitude in second bunching cavity as a function of drive frequency for B = 32 kG and q = 0.3.

OUTPUT CAVITY AXIAL PROFILE FUNCTION

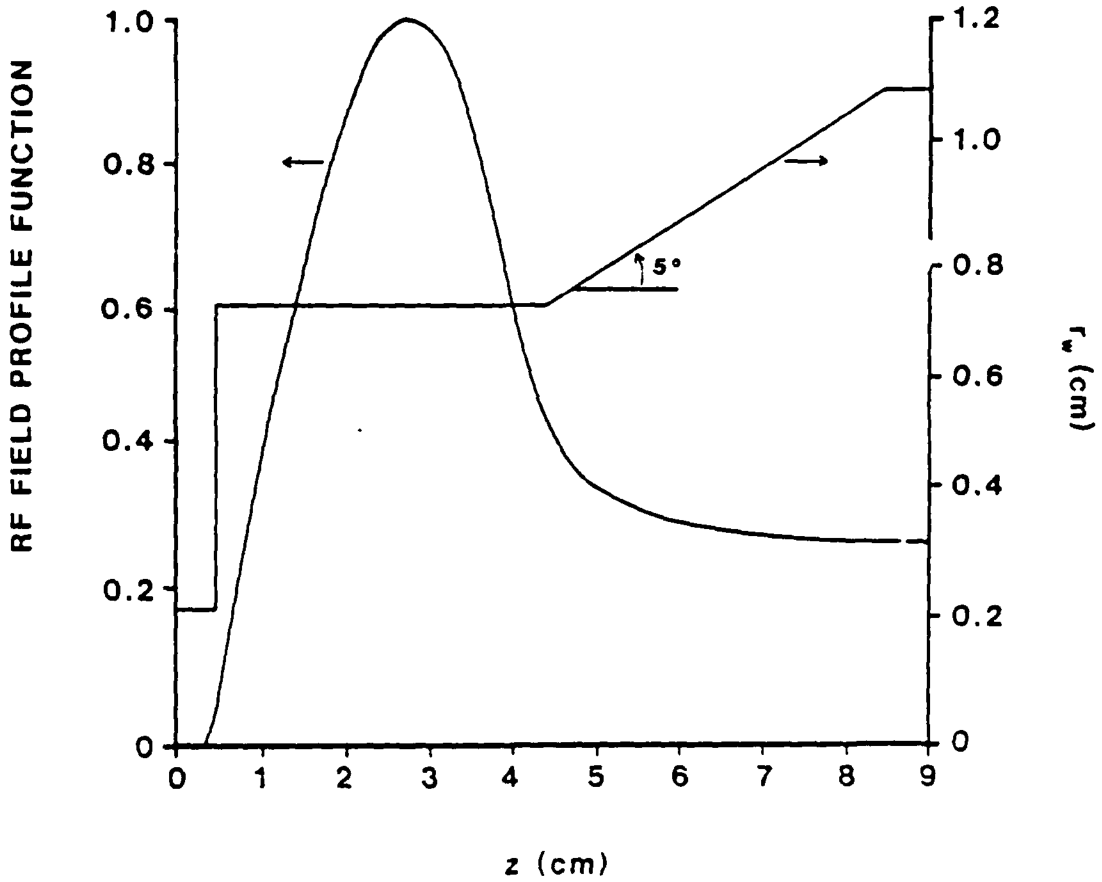

Fig. 11. Axial RF field profile for TE_{121} output cavity.

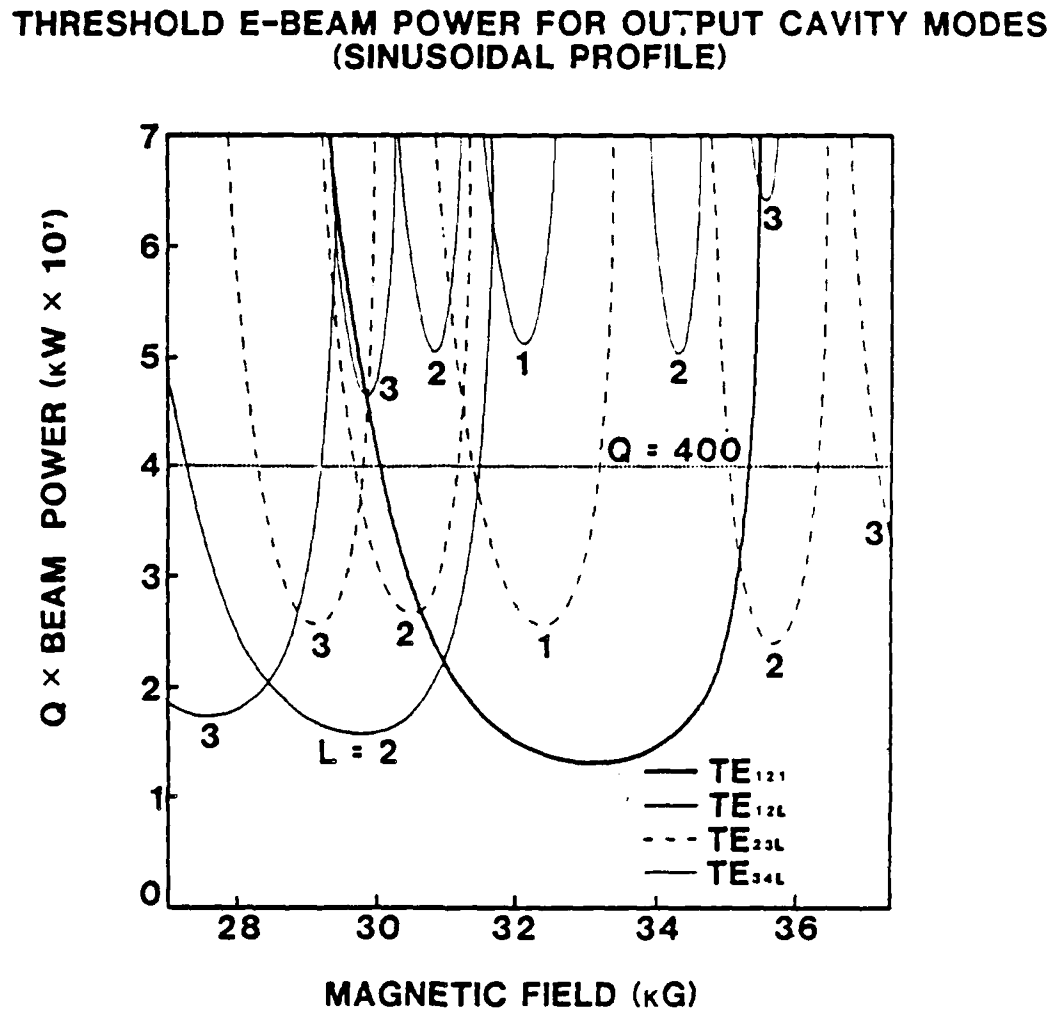

Fig. 12. Scan of Q × threshold beam power for the TE_{121} mode and competing modes in the output cavity. The calculations assume a sinusoidal axial profile, circular polarization, $L/\lambda=4.5$, and $\alpha=0.75$. The TE_{12} modes interact at the first harmonic, the TE_{23} modes interact at the second harmonic, and the TE_{34} modes interact at the third harmonic.

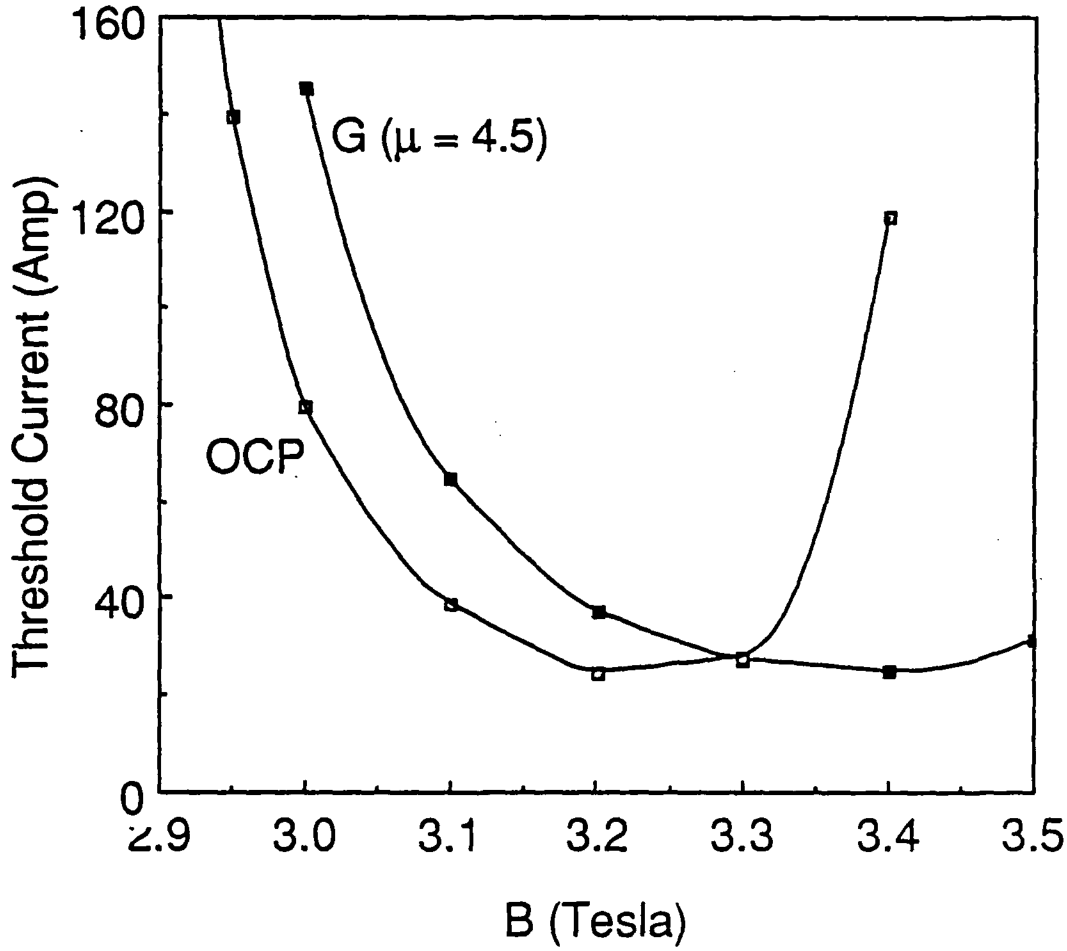

Fig. 13. Oscillation threshold current of TE_{121} mode in output cavity based on realistic open cavity RF field profile (OCP) and on a gaussian profile (G) with μ=4.5.

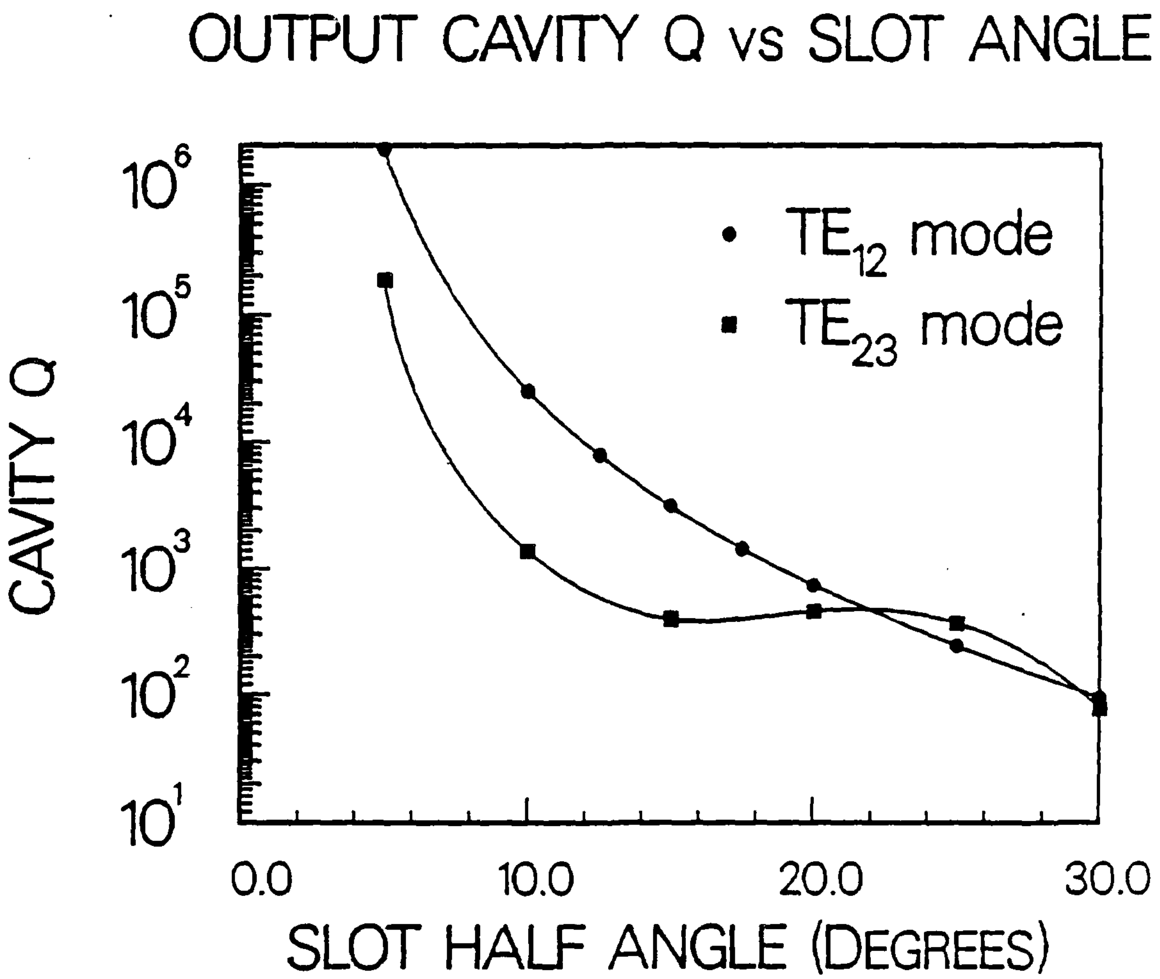

Fig. 14. Calculated slot Q-value vs slot half-angle for the TE_{12} and TE_{23} modes of the output cavity.

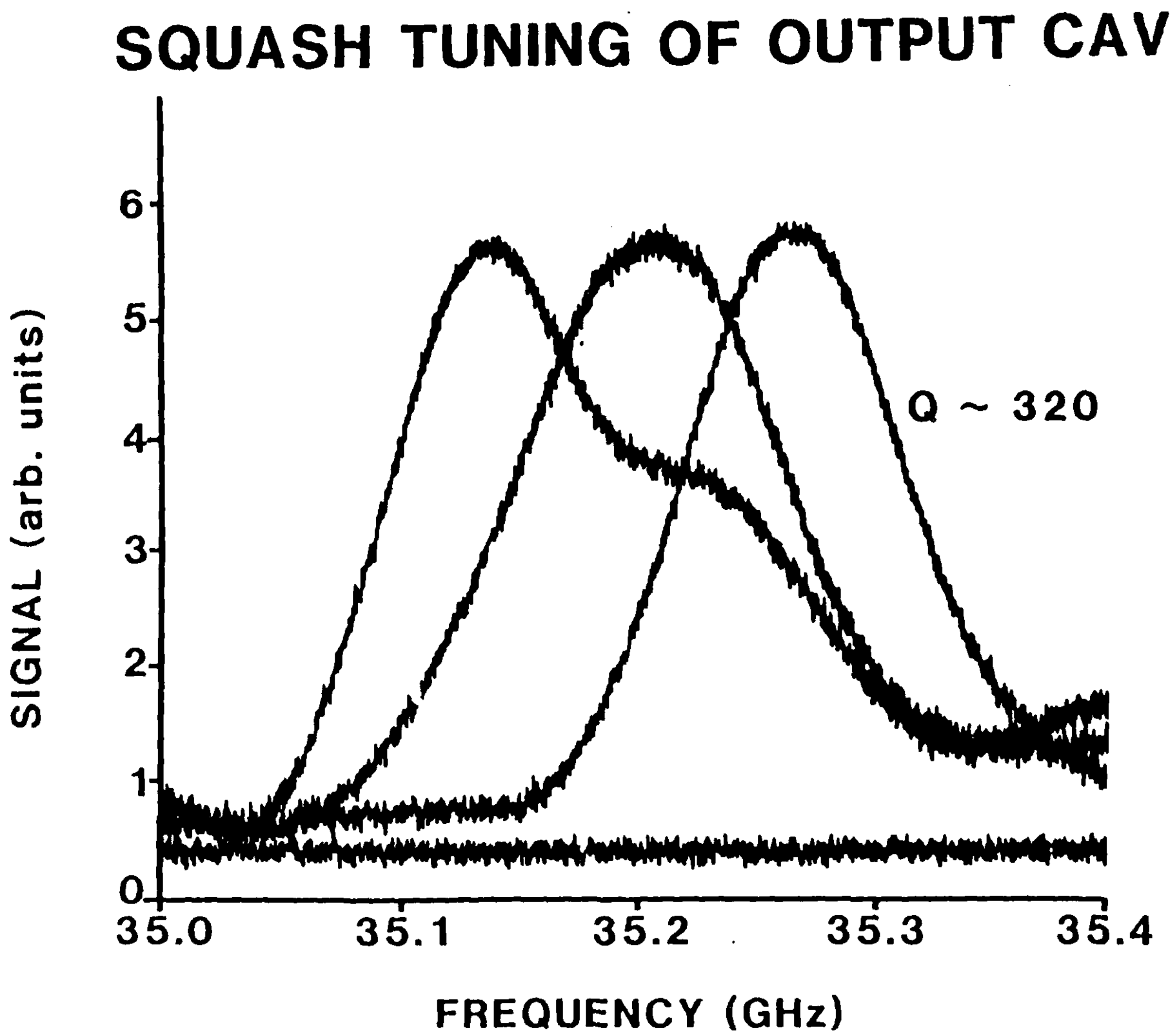

Fig. 15. Cold test of the TE_{121} resonance of the output cavity, illustrating the effect of "squash-tuning" of the cavity frequency.

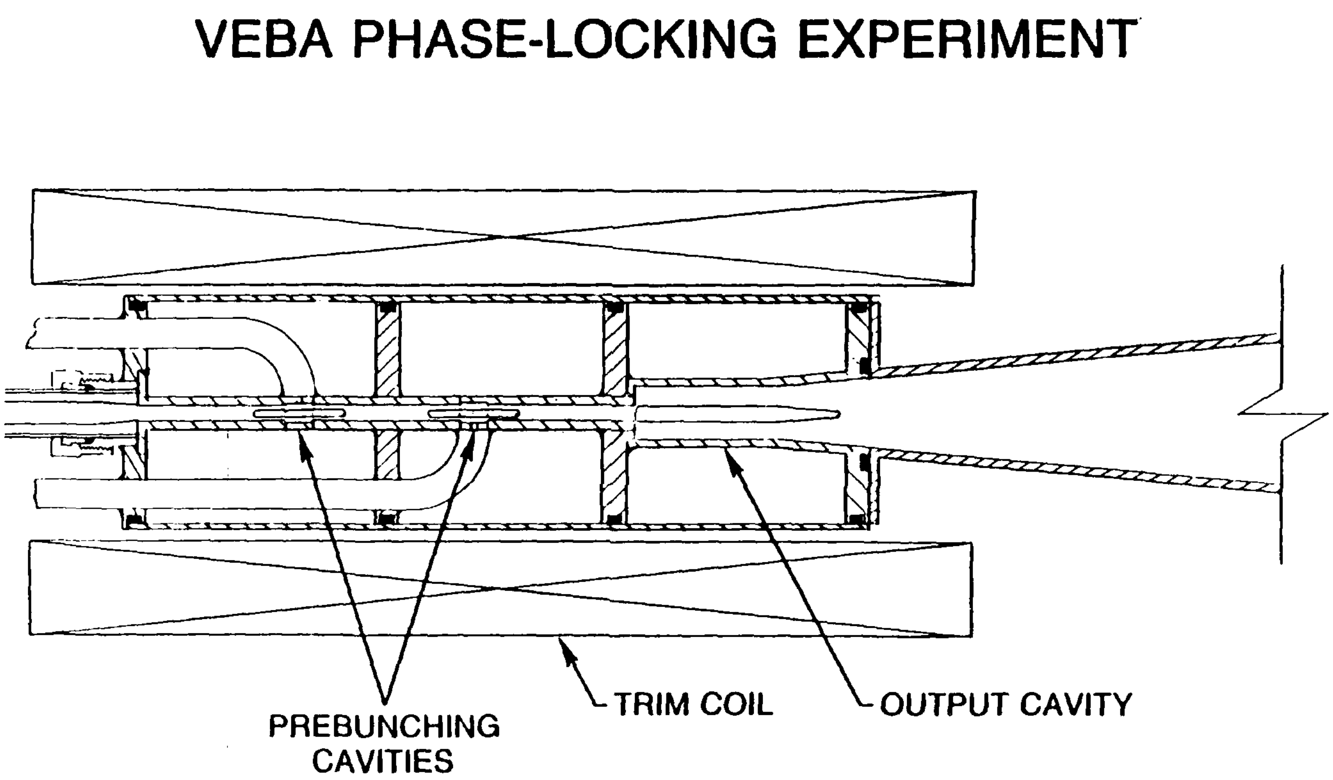

Fig. 16. Scale dra ing of the two prebunching cavities, the output cavity, and the drift sections of the three-cavity phase-locking experiment.

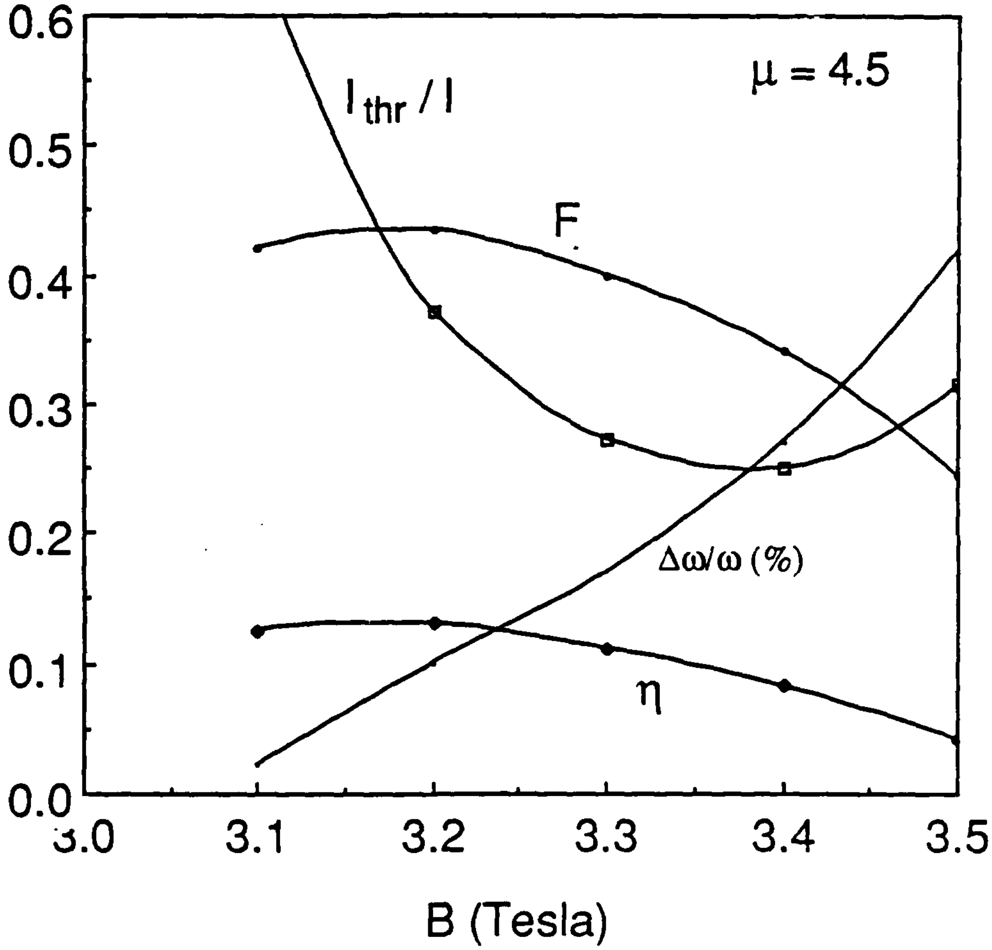

Fig. 17. Free-running oscillator parameters as a function of magnetic field for the output cavity operating in the TE_{121} mode and a beam current of 100 Amp.

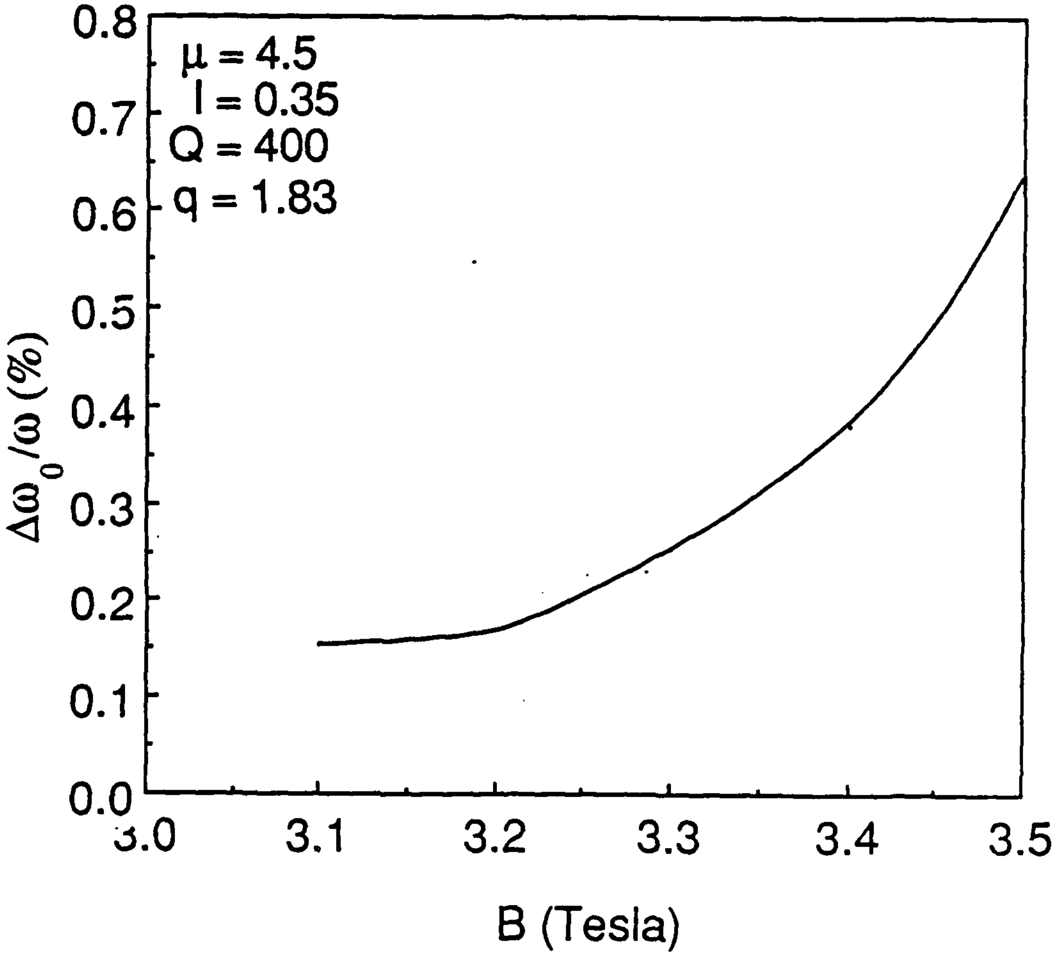

Fig. 18. Maximum phase-locking bandwidth obtainable using optimally prebunched beam based on perturbation theory.

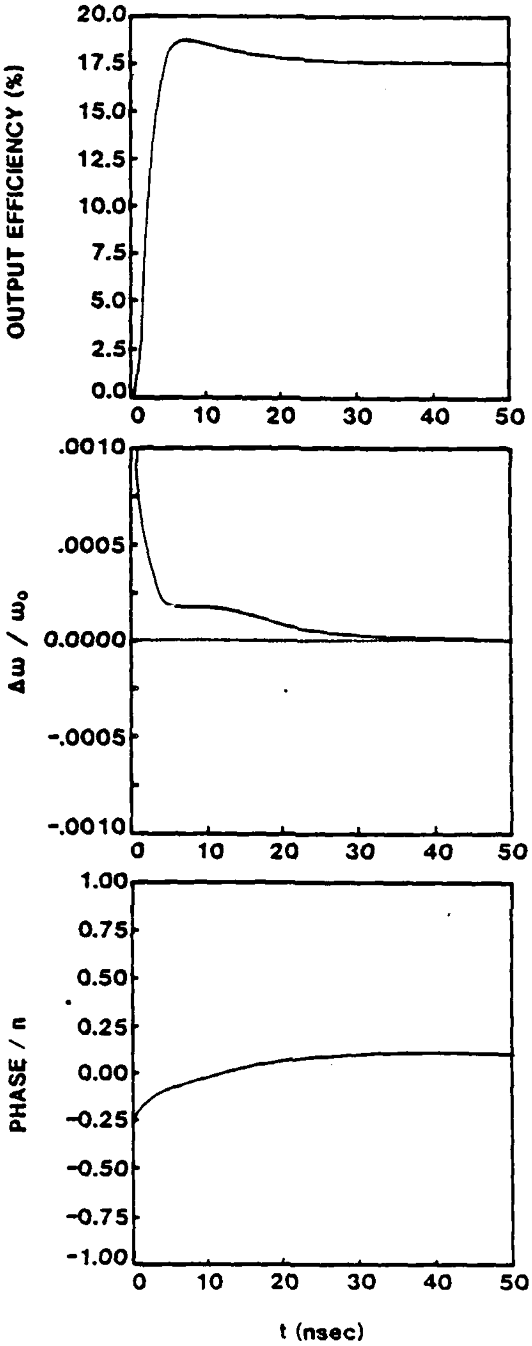

Fig. 19. Time evolution of output cavity efficiency, operating frequency, and RF phase during phase-locked operation. The calculation assumes a flat voltage pulse, $q_3=2.0$, a magnetic field of 32 kG, a gaussian profile with $\mu=4.5$, and a locking frequency shift $\Delta\omega_0/\omega_0=0.1\%$.

TIME EVOLUTION OF PHASE-LOCKED GYROTRON

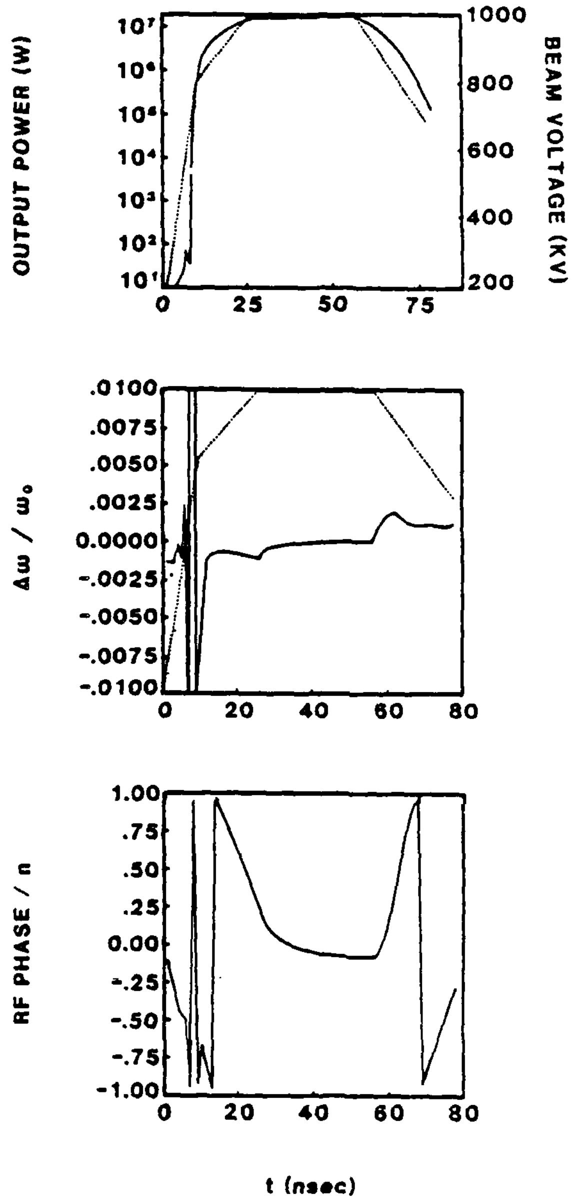

Fig. 20. Time evolution of output cavity efficiency, operating freauency, and RF phase during phase-locked operation. The calculation assumes a typical, somewhat smoothed, VEBA voltage pulse, q_3=2.0, a magnetic field of 32 kG, a gaussian axial profile with μ=4.5, and a locking frequency shift $\Delta\omega_0/\omega_0$=0.1%.

<u>4740 DISTRIBUTION LIST</u>

Air Force Avionics Laboratory AFWAL/AADM-1 Wright/Patterson AFB, Ohio 45433 Attn: Walter Friez	1 copy
Air Force Office of Scientific Research Bolling AFB Washington, D.C. 20332 Attn: H. Schlossberg	1 copy
Air Force Weapons Lab Kirkland AFB Albuquerque, New Mexico 87117 Attn: Dr. William Baker	2 copies
Columbia University 520 West 120th Street Department of Electrical Engineering New York, N.Y. 10027 Attn: Dr. S.P. Schlesinger	1 copy
A. Sen	1 copy
Columbia University 520 West 120th Street Department of Applied Physics and Nuclear Engineering New York, New York 10027 Attn: T.C. Marshall	1 copy
R. Gross	1 copy
Cornell University School of Applied and Er.ineering Physics Ithica, New York 14853 Attn: Prof. Hans H. Fleischmann	1 copy
John Nation	1 copy
R. N. Sudan	1 copy
Dartmouth College 18 Wilder, Box 6127 Hanover, New Hampshire 03755 Attn: Dr. John E. Walsh	1 copy
Department of Energy The Pentagon Washington, D.C. 20545 Attn: C. Finfgeld/ER-542, GTN	1 copy
T.V. George/ER-531, GTN	1 copy
D. Crandall/ER-55, GTN	1 copy

Defense Advanced Research Project Agency/DEO 1400 Wilson Blvd. Arlington, Virginia 22209	
Attn: Dr. S. Shey	1 copy
Dr. L. Buchanan	1 copy
Defense Communications Agency Washington, D.C. 20305 Attn: Dr. Pravin C. Jain Assistant for Communications Technology	1 copy
Defense Nuclear Agency Washington, D.C. 20305	
Attn: Mr. J. Farber	1 copy
Mr. Lloyd Stossell	1 copy
Dr. Leon Wittwer (RAAE)	5 copies
Defense Technical Information Center Cameron Station 5010 Duke Street Alexandria, Virginia 22314	2 copies
Georgia Tech. EES-EOD Baker Building Atlanta, Georgia 30332 Attn: Dr. James J. Gallagher	1 copy
Hanscomb Air Force Base Stop 21, Massachusetts 01731 Attn: Lt. Rich Nielson/ESD/INK	1 copy
Hughes Aircraft Co. Electron Dynamics Division 3100 West Lomita Boulevard Torrance, California 90509	
Attn: J. Christiansen	1 copy
J.J. Tancredi	1 copy
KMS Fusion, Inc. 3941 Research Park Dr. P.O. Box 1567 Ann Arbor, Michigan 48106 Attn: S.B. Segall	1 copy
Lawrence Livermore National Laboratory P.O. Box 808 Livermore, California 94550	
Attn: Dr. D. Prosnitz	1 copy
Dr. T.J. Orzechowski	1 copy
Dr. J. Chase	1 copy

Los Alamos Scientific Laboratory	
P.O. Box 1663, AT5-827	
Los Alamos, New Mexico 87545	
Attn: Dr. J.C. Goldstein	1 copy
Dr. T.J.T. Kwan	1 copy
Dr. L. Thode	1 copy
Dr. C. Brau	1 copy
Dr. R. R. Bartsch	1 copy
Massachusetts Institute of Technology	
Department of Physics	
Cambridge, Massachusetts 02139	
Attn: Dr. G. Bekefi/36-213	1 copy
Dr. M. Porkolab/NW 36-213	1 copy
Dr. R. Davidson/NW 16-206	1 copy
Dr. A. Bers/NW 38-260	1 copy
Dr. K. Kreischer	1 copy
Massachusetts Institute of Technology	
167 Albany St., N.W. 16-200	
Cambridge, Massachusetts 02139	
Attn: Dr. R. Temkin/NW 14-4107	1 copy
Spectra Technologies	
2755 Northup Way	
Bellevue, Washington 98004	
Attn: Dr. J.M. Slater	1 copy
Mission Research Corporation	
Suite 201	
5503 Cherokee Avenue	
Alexandria, Virginia 22312	
Attn: Dr. M. Bollen	1 copy
Dr. Tom Hargreaves	1 copy
Mission Research Corporation	
1720 Randolph Road, S.E.	
Albuquerque, New Mexico 87106	
Attn: Dr. Ken Busby	1 copy
Mr. Brendan B. Godfrey	1 copy
SPAWAR	
Washington, D.C. 20363	
Attn: E. Warden	
Code PDE 106-3113	1 copy
G. Bates	
PMW 145	1 copy
Naval Research Laboratory	
Addressee: Attn: Name/Code	
Code 1001 - T. Coffey	1 copy
Code 1220 - Security	1 copy
Code 2628 - TID Distribution	22 copies
Code 4000 - W. Ellis	1 copy
Code 4700 - S. Ossakow	26 copies

Code 4700.1 - A.W. Ali	1 copy
Code 4710 - C. Kapetanakos	1 copy
Code 4740 - Branch Office	25 copies
Code 4740 - W. Black	1 copy
Code 4740 - A. Fliflet	1 copy
Code 4740 - S. Gold	1 copy
Code 4740 - A. Kinkead	1 copy
Code 4740 - W.M. Manheimer	1 copy
Code 4740 - M. Rhinewine	1 copy
Code 4770 - G. Cooperstein	1 copy
Code 4790 - B. Hui	1 copy
Code 4790 - C.M. Hui	1 copy
Code 4790 - Y.Y. Lau	1 copy
Code 4790 - P. Sprangle	1 copy
Code 5700 - L.A. Cosby	1 copy
Code 6840 - S.Y. Ahn	1 copy
Code 6840 - A. Ganguly	1 copy
Code 6840 - R.K. Parker	1 copy
Code 6840 - N.R. Vanderplaats	1 copy
Code 6850 - L.R. Whicker	1 copy
Code 6875 - R. Wagner	1 copy

Naval Sea Systems Command
Department of the Navy
Washington, D.C. 20362
Attn: Commander George Bates
PMS 405-300 — 1 copy

Northrop Corporation
Defense Systems Division
600 Hicks Rd.
Rolling Meadows, Illinois 60008
Attn: Dr. Gunter Dohler — 1 copy

Oak Ridge National Laboratory
P.O. Box Y
Mail Stop 3
Building 9201-2
Oak Ridge, Tennessee 37830
Attn: Dr. A. England — 1 copy

Office of Naval Research
800 N. Quincy Street
Arlington, Va. 22217
Attn: Dr. C. Roberson — 1 copy
Dr. W. Condell — 1 copy
Dr. T. Berlincourt — 1 copy

Office of Naval Research
1030 E. Green Street
Pasadena, CA 91106
Attn: Dr. R. Behringer — 1 copy

Optical Sciences Center University of Arizona Tucson, Arizona 85721 Attn: Dr. Willis E. Lamb, Jr.	1 copy
OSD/SDIO Washington, D.C. 20301-7100 Attn: IST (Dr. H. Brandt)	1 copy
Pacific Missile Test Center Code 0141-5 Point Muga, California 93042 Attn: Will E. Chandler	1 copy
Physical Dynamics, Inc. P.O. Box 10367 Oakland, California 94610 Attn: A. Thomson	1 copy
Physics International 2700 Merced Street San Leandro, California 94577 Attn: Dr. J. Benford	1 copy
Physical Science Inc. 603 King Street Alexandria, VA 22314 ATTN: M. Read	1 copy
Princeton Plasma Plasma Physics Laboratory James Forrestal Campus P.O. Box 451 Princeton, New Jersey 08544 Attn: Dr. H. Hsuan	2 copies
Dr. J. Doane	1 copy
Dr. D. Ignat	1 copy
Dr. H. Furth	1 copy
Dr. P. Efthimion	1 copy
Dr. F. Perkins	1 copy
Quantum Institute University of California Santa Barbara, California 93106 Attn: Dr. L. Elias	1 copy
Raytheon Company Microwave Power Tube Division Foundry Avenue Waltham, Massachusetts 02154 Attn: N. Dionne	1 copy

Sandia National Laboratories
ORG. 1231, P.O. Box 5800
Albuquerque, New Mexico 87185
Attn: Dr. Thomas P. Wright 1 copy
Mr. J.E. Powell 1 copy
Dr. J. Hoffman 1 copy
Dr. W.P. Ballard 1 copy
Dr. C. Clark 1 copy

Science Applications, Inc.
1710 Goodridge Dr.
McLean, Virginia 22102
Attn: Adam Drobot 1 copy
P. Vitrello 1 copy
D. Bacon 1 copy
C. Menyuk 1 copy

Stanford University
High Energy Physics Laboratory
Stanford, California 94305
Attn: Dr. T.I. Smith 1 copy

TRW, Inc.
Space and Technology Group
Suite 2600
1000 Wilson Boulevard
Arlington, VA 22209
Attn: Dr. Neil C. Schoen 1 copy

TRW, Inc.
Redondo Beach, California 90278
Attn: Dr. H. Boehmer 1 copy
Dr. T. Romisser 1 copy

University of California
Physics Department
Irvine, California 92717
Attn: Dr. G. Benford 1 copy
Dr. N. Rostoker 1 copy

University of California
Department of Physics
Los Angeles, CA 90024
Attn: Dr. A.T. Lin 1 copy
Dr. N. Luhmann 1 copy
Dr. D. McDermott 1 copy

University of Maryland
Department of Electrical Engineering
College Park, Maryland 20742
Attn: Dr. V. L. Granatstein 1 copy
Dr. W. W. Destler 1 copy

University of Maryland
Laboratory for Plasma and Fusion
Energy Studies
College Park, Maryland 20742
Attn: Dr. Tom Antonsen 1 copy
Dr. John Finn 1 copy
Dr. Jhan Varyan Hellman 1 copy
Dr. Baruch Levush 1 copy
Dr. John McAdoo 1 copy
Dr. Edward Ott 1 copy

University of Tennessee
Dept. of Electrical Engr.
Knoxville, Tennessee 37916
Attn: Dr. I. Alexeff 1 copy

University of New Mexico
Department of Physics and Astronomy
800 Yale Blvd, N.E.
Albuquerque, New Mexico 87131
Attn: Dr. Gerald T. Moore 1 copy

University of Utah
Deparment of Electrical Engineering
3053 Merrill Engineering Bldg.
Salt Lake City, Utah 84112
Attn: Dr. Larry Barnett 1 copy
Dr. J. Mark Baird 1 copy

U. S. Naval Academy
Annapolis, Maryland 21402-5021 1 copy

U. S. Army
Harry Diamond Labs
2800 Powder Mill Road
Adelphi, Maryland 20783-1145
Attn: Dr. Howard Brandt 1 copy
Dr. Edward Brown 1 copy
Dr. Stuart Graybill 1 copy

Varian Associates
611 Hansen Way
Palo Alto, California 94303
Attn: Dr. H. Jory 1 copy
Dr. David Stone 1 copy
Dr. Kevin Felch 1 copy
Dr. A. Salop 1 copy

Varian Eimac San Carlos Division
301 Industrial Way
San Carlos, California 94070
Attn: C. Marshall Loring 1 copy

Yale University
Applied Physics
Madison Lab
P.O. Box 2159
Yale Station
New Haven, Connecticut 06520
Attn: Dr. N. Ebrahim 1 copy
Dr. I. Bernstein 1 copy

Records 1 copy

Cindy Sims Code 2634 1 copy